An Explicit Finite Element Modelling Method for Masonry Walls under Out-of-plane Loading

Sarkar Noor-E-Khuda, Manicka Dhanasekar[1] and David P Thambiratnam

Queensland University of Technology (QUT), Brisbane, Australia.

Abstract

An explicit finite element modelling method is formulated using a layered shell element to examine the behaviour of masonry walls subject to out-of-plane loading. Masonry is modelled as a homogenised material with distinct directional properties that are calibrated from datasets of a "C" shaped wall tested under pressure loading applied to its web. The predictions of the layered shell model have been validated using several out-of-plane experimental datasets reported in the literature. Profound influence of support conditions, aspect ratio, pre-compression and opening to the strength and ductility of masonry walls is exhibited from the sensitivity analyses performed using the model.

Keywords: Explicit finite element model; Out-of-plane; Masonry; Macroscopic material; shell element; Pre-compression

[1] Corresponding Author: M. Dhanasekar, Professor, School of Civil Engineering and Built Environment, Queensland University of Technology, S-714, Gardens Point Campus, Brisbane, QLD4001. Ph. +61 7 3138 6666; Fax. +61 7 3138 1170; email: m.dhanasekar@qut.edu.au

Nomenclature

A	Area	α	Shear stress contribution factor to the tension failure
A_0	Initial area of reference surface	α_g	Mathematical variable for plastic flow of masonry
a	Current area after loading	β	Biaxial compressive strength factor
B	Strain deformation transformation matrix	γ	Shear stress contribution factor to compression failure
b	Damping coefficient	$\bar{\gamma}^{ts}$	Transverse shear strain
c_d	Current dilatational wave speed	$\bar{\gamma}_0^{ts}$	Transverse shear strain at centre of element
Cs	Curvilinear component of transverse shear stiffness	$\bar{\gamma}_x^{ts}, \bar{\gamma}_y^{ts}$	Components of transverse shear strain
c_α, c_β	Element distortion coefficients	$\gamma_x^E, \gamma_x^F, \gamma_y^G, \gamma_y^H$	Covariant transverse shear strains evaluated at the mid points E,F,G,H respectively of the element boundary
E_n	Young's Modulus of masonry normal to bed joints	γ_{bf}	Strain associated with butterfly deformation pattern
E_p	Young's Modulus of masonry parallel to bed joints	γ_{cc}	Strain associated with crop circle pattern
E_z	Young's Modulus of masonry along thickness direction	γ_{hg}	Hourglass transverse shear strain vector
f	Body force Vector	λ', μ'	Effective Lame's constant
f_{cn}	Compressive strength normal to bed joint	Δ_u	Ultimate displacement
f_{cp}	Compressive strength parallel to bed joints	Δ_y	Yield displacement
f_{cy}	Compressive strength of masonry	$\Delta\varepsilon$	Strain increment
f_{tn}	Tensile strength normal to bed joints	$\Delta\varepsilon_{vol}$	Volumetric strain rate
f_{tp}	Tensile strength parallel to bed joints	$\Delta\varepsilon_{xx}, \Delta\varepsilon_{xy}, \Delta\varepsilon_{yy}$	Strain increment
F_u	Ultimate force	$\Delta\bar{\varepsilon}_{xx}, \Delta\bar{\varepsilon}_{xy}, \Delta\bar{\varepsilon}_{yy}$	Reference surface strain increment
$\bar{f}_{zz}$	Thickness increase factor used to identify integration points through element thickness	$\Delta\kappa$	Curvature increment
G	Shear modulus of masonry	$\Delta\kappa_{xx}, \Delta\kappa_{yy}, \Delta\kappa_{xy}$	Curvature increment along local x – and y – direction and xy plane
G_{fcn}	Energy for compression failure normal to bed joints	Δt	Time step size
G_{fcp}	Energy for compression failure parallel to bed joints	$\varepsilon_{xx}, \varepsilon_{yy}, \varepsilon_{xy}$	Strain components along local x – and y – direction and xy plane
G_{ftn}	Fracture energy normal to bed joints	$\bar{\varepsilon}_{xx}, \bar{\varepsilon}_{yy}, \bar{\varepsilon}_{xy}$	Reference surface strain components
G_{ftp}	Fracture energy parallel to bed joints	ε_z	Strain component along thickness direction
G_{xz}, G_{yx}	Shear Moduli in the out-of-plane direction	κ_c	Scalar control hardening and softening under compression
H	Height of wall	κ_t	Scalar control tension softening
h	Changed thickness of element (mm) under loading	$\bar{\kappa}_{xy}$	Reference surface curvature
h_o	Initial thickness of element (mm)	μ	Displacement Ductility
K_0	Initial stiffness of wall	ν_n	Poisson's ratio of masonry normal to bed joints
K_{xx}^{ts}, K_{yy}^{ts}, $\bar{K}_{xy}$	Actual section shear stiffness along x and y direction and xy plane	ν_p	Poisson's ratio of masonry parallel to bed joints
K_{xy}^{ts}	Actual section shear stiffness along xy plane	ν_z	Poisson's ratio of masonry along thickness
L	Length of wall	ρ	Mass density

$L_c(mm)$	Characteristic length of critical elements
l_x, l_y	Change of length of element along x – and y- direction
$l^o{}_x, l^o{}_y$	Initial length of element along x – and y - direction
M	Mass matrix
$\overline{M}$	Moment
m	Bulk viscosity pressure
$\tilde{m}$	Normalised moment
N	Shape function
Q	Resultant transverse shear force
Q^x, Q^y	Components of transverse shear forces
q^x, q^y	True transverse shear force components in shell orthonormal coordinate system
R	Rotary inertia scaling
r	Parameter that defines shape of $(\overline{M} - \varphi)$ curve
S	Surface of finite body
S_z	Coordinate in thickness direction
t	External traction
U	Internal energy
u^n	Displacement of body
$\dot{u}^n$	Velocity
$\ddot{u}^n$	Acceleration
u_x, u_y, u_z	Displacement along local x,y,z direction, respectively
V	Volume of element
V_o	Initial volume of element
W	External work done

ρ_{bv}	Linear bulk viscosity pressure
ρ_{io}	ith element reference density
$\tau_{u,c}$	Pure shear strength
$\tau_{pn}, \tau_{po}, \tau_{no}$	Shear stress components
σ	Stress
$\overline{\sigma}_{cn}, \overline{\sigma}_{cp}$	Exponential compressive softening parameter along the normal and the parallel to bed joint directions, respectively
σ_n	Normal stress component normal to masonry bed joint
σ_p	Normal stress component parallel to masonry bed joint
σ_t	Equivalent stress to define the softening behaviour
$\overline{\sigma}_{tn}, \overline{\sigma}_{tp}$	Exponential tensile softening parameter along the normal and the parallel to bed joint directions, respectively
σ_v	Vertical pre-compression
σ_z	Stress component perpendicular to mid-plane
θ_x, θ_y	Rotation about x and y direction
θ_z	Rotation about shell normal
φ	Curvature
$\tilde{\varphi}$	Normalised curvature
$\tilde{\varphi}_o$	Normalised curvature at maximum moment

1. Introduction

Masonry is vastly used in the construction of structural and non-structural walls. In cyclonic and seismic events masonry buildings experience a combination of in-plane and out-of-plane loading. Past researches [1-4] primarily focused on the in-plane shear behaviour of masonry walls, being the prime load path in the lateral load transfer mechanism. On the contrary the out-of-plane loading requires sufficient out-of-plane capacity to avoid partial or full failure of the walls, which leads to un-reparable damages to buildings and in many cases causalities due to falling debris. Recent studies [5, 6] identified the out-of-plane collapse as one of the common failure mechanisms of masonry walls. Most studies on the out-of-plane behaviour of masonry walls are limited to experimental methods, which are expensive and time consuming. With the advent of high power computers, finite element methods offer economic and elegant alternate approach to the experimental counterpart. This paper presents an explicit finite element (EFE) modelling method, which provides highly stable solutions even after a series of adjacent elements fail and lose their stiffness provided the kinetic energy remains significantly lower than the internal energy in the static problems such as the one attended to in this paper. Although this paper predominantly deals with the static pressure loading normal to the plane of walls, the explicit modelling method formulated herein can be extended to the vehicular impacts and blast loadings on masonry facades that have become a source of concerns in recent times as demonstrated in [7] using experimental and EFE modelling using LS-DYNA. In this paper the formulated EFE modelling is incorporated into ABAQUS/EXPLICIT.

The accuracy of the EFE analysis largely depends on the time step definition of proper material properties and the discretisation of the continuum. Masonry comprises of a series of blocks/units connected through binder materials along its bed and head joints. Therefore, masonry displays distinct orthotropic tensile and compressive strengths, stiffness and post-peak softening features, which depend on its constitutive materials including the mode of construction.

To date most FE modelling techniques have considered masonry as a two-dimensional plane stress continuum [1, 2, 8] suitable for the prediction of the in-plane shear and compression responses. Out-of-plane flexural behaviour modelling requires definition of curvature (rotational) that can be obtained only in a three-dimensional space. Analytical models were developed [9-11] to predict the out-of-plane response of the unreinforced masonry (URM)

walls. [10] proposed a simplified procedure to model the moment-curvature relationship of URM walls. Out-of-plane response requires investigation of full scale specimen of practicable dimensions to appropriately establish its moment-curvature relation, and hence micro modelling approach would be very expensive as demonstrated in [12-15]. In this paper masonry is treated as a macroscopic homogenised material suitable for incorporation into shell element. A 3D thin shell element capable of predicting the flexural behaviour without shear locking is adopted for this study.

To overcome the computational costs, masonry is considered as a single homogenised material [8, 16-18] that includes the units and the mortar bed and head joints with embedded interfaces allowing for tensile and shear bond failures. A 3D failure surface in the plane stress space normal stresses parallel and normal to an axis parallel to bed joint and the shear stress in a plane defined by the bed and head joints) of masonry suitable for uniaxial and biaxial tension/compression is reported in [19]. [20] provided a damage-plasticity framework to the failure surface and successfully developed a homogenised macro model for masonry in the plane stress space; this model was extended for reinforced masonry by [1] through a VUMAT subroutine suitable for ABAQUS explicit algorithm and used for the analysis of URM and wide spaced reinforced masonry, confined masonry [3] and walls with high bond strength mortar joints [4]. The present study has extended the VUMAT algorithm suitable for 3D shell elements so that both the in-plane and the out-of-plane behaviours of masonry walls could be simulated.

This paper describes the macro-modelling method to determine the out-of-plane response of URM walls. A number of test datasets have been collected from the literature to calibrate the material parameters in the VUMAT subroutine developed for the shell elements and validate the predictions of the EFE model containing the VUMAT subroutine. Finally some parametric studies have been conducted to extend the knowledge on the behaviour of out-of-plane loaded walls.

2. Material Description

The strain components are linearly distributed across the thickness direction of the elastic shell and can be related to its mid surface strains. As integral of stresses through the shell thickness of shell vanishes, the variation of stresses with respect to the thickness direction gives rise to a 2D theory of shells used in the assessment of its out-of-plane response. In this

study, masonry is modelled using the multi-surface plasticity model that contains a Rankine type yield surface for tension and a Hill type orthotropic yield surface for compression. The Rankine failure criteria can be written as in (1),

$$f_1 = \frac{\left(\sigma_p - \bar{\sigma}_{tp}(\kappa_t)\right) + \left(\sigma_n - \bar{\sigma}_{tn}(\kappa_t)\right)}{2} + \sqrt{\left(\frac{\left(\sigma_p - \bar{\sigma}_{tp}(\kappa_t)\right) - \left(\sigma_n - \bar{\sigma}_{tn}(\kappa_t)\right)}{2}\right)^2 + \alpha\tau_{pn}} \quad (1)$$

Where, scalar κ_t controls the amount of tension softening. Shear stress contribution to tension failure of masonry material is defined by (2),

$$\alpha = \frac{f_{tp} f_{tn}}{\tau_{pn}^2} \quad (2)$$

where f_{tp}, f_{tn} and τ_{pn} are the uniaxial tensile strength parallel and normal to bed joint and pure shear strength, respectively. Exponential tensile softening parameters ($\bar{\sigma}_{tp}$ and $\bar{\sigma}_{tn}$) which act along the directions parallel and perpendicular to bed joint, are calculated using the expressions (3),

$$\bar{\sigma}_{tp} = f_{tp} e^{\left(-\frac{L_c f_{tp}}{G_{ftp}}\kappa_t\right)}, \quad \bar{\sigma}_{tn} = f_{tn} e^{\left(-\frac{L_c f_{tn}}{G_{ftn}}\kappa_t\right)} \quad (3)$$

For solid clay block masonry, $\alpha \approx 1.1$ and $f_{tn}/f_{tp} \approx 0.5$ was adopted in the calibration phase [20].

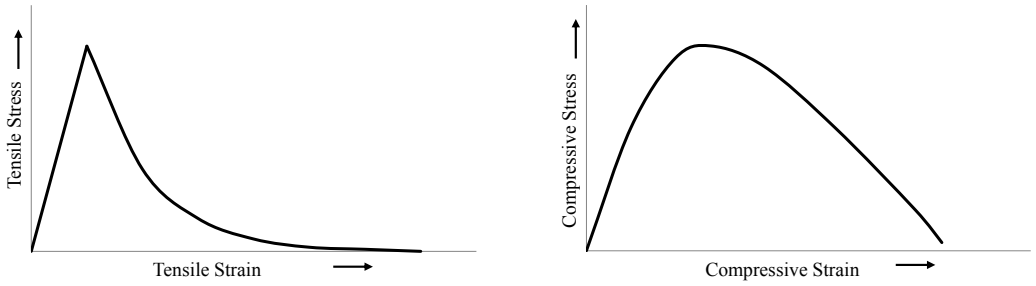

(a) (b)

Fig. 1 Response of masonry to uniaxial (a) Tension, (b) Compression

The Hill type yield surface for the shell formulation is written as in (4),

$$f_2 = A\sigma_p^2 + B\sigma_p\sigma_n + C\sigma_n^2 + D\left(\tau_{pn}^2 + \tau_{po}^2 + \tau_{no}^2\right) - 1 = 0 \quad (4)$$

where,

$$A=\frac{1}{\left(\bar{\sigma}_{cp}(\kappa_c)\right)^2},\ B=\frac{\beta}{\left(\bar{\sigma}_{cp}(\kappa_c)\bar{\sigma}_{cn}(\kappa_c)\right)},\ C=\frac{1}{\left(\bar{\sigma}_{cn}(\kappa_c)\right)^2},\ D=\frac{\gamma}{\left(\bar{\sigma}_{cp}(\kappa_c)\bar{\sigma}_{cn}(\kappa_c)\right)} \tag{5}$$

Here A, B, C, D are material parameters for the shell formulation and the suffix p, n and o represents parallel and perpendicular to bed joints and the out-of-plane thickness directions, respectively.

Scalar κ_c controls the hardening and softening under compression; whereas the parameters β and γ control the coupling between normal stress and shear stress contribution to failure, which can be determined from the biaxial and uniaxial compression tests, respectively. γ is given by (6) where, $\tau_{u,c}$ is material pure shear strength.

$$\left(\gamma=\frac{f_{cp}f_{cn}}{\tau_{u,c}^2}\right) \tag{6}$$

In the absence of such a test, β = -1.0 and $\gamma = 4$ [20] was considered for solid clay block masonry. One of the key aspects of macro modelling is its dependence on mesh size due to localisation of stresses of the smeared material definition. A simplified approach is adopted to compensate for mesh pathology using a single length parameter known as the characteristic length for elements L_c calculated as the square root of the area of the element as such each element of mesh consists of some part of the mortar and block which yields physically consistent results.

The material model has been incorporated into the ABAQUS/ EXPLICIT program through a VUMAT subroutine coded in FORTRAN. A total of 21 material constants are required for the VUMAT model; these constants are discussed further with reference to numerical examples in Sections 4 and 5 of this paper.

3. Explicit Finite Element Model

The EFE modelling is defined using shell elements, therefore it can deal with the in-plane and the out-of-plane loading as well as the combination of the two; an example problem reported in this paper contains a main wall with two return walls attached to its two vertical edges. A 4-noded 24-DOF quadrilateral finite-membrane-strain element is used in this study [Fig. 2].

The strain increment $(\Delta\varepsilon)$ at a point through the thickness of the S4R element, shown in (7), is given in terms of the physical curvature increment $(\Delta\kappa)$ of the element.

$$\left.\begin{aligned}\Delta\varepsilon_{xx} &= \Delta\bar{\varepsilon}_{xx} + \bar{f}_{zz}^{t+\Delta t} S_z \Delta\kappa_{xx} \\ \Delta\varepsilon_{xy} &= \Delta\bar{\varepsilon}_{xy} + \bar{f}_{zz}^{t+\Delta t} S_z \Delta\kappa_{xy} \\ \Delta\varepsilon_{yy} &= \Delta\bar{\varepsilon}_{yy} + \bar{f}_{zz}^{t+\Delta t} S_z \Delta\kappa_{yy}\end{aligned}\right\} \tag{7}$$

Here, $\Delta\bar{\varepsilon}_{xy}$ represents the reference surface strain increment. The thickness increase factor $\bar{f}_{zz}$ which is independent of coordinate in thickness direction and S_z is used to identify the position of material point along the shell thickness. The analysis is carried out with relax stiffness hourglass control, default element deletion and maximum degradation control to reduce numerical complicacies.

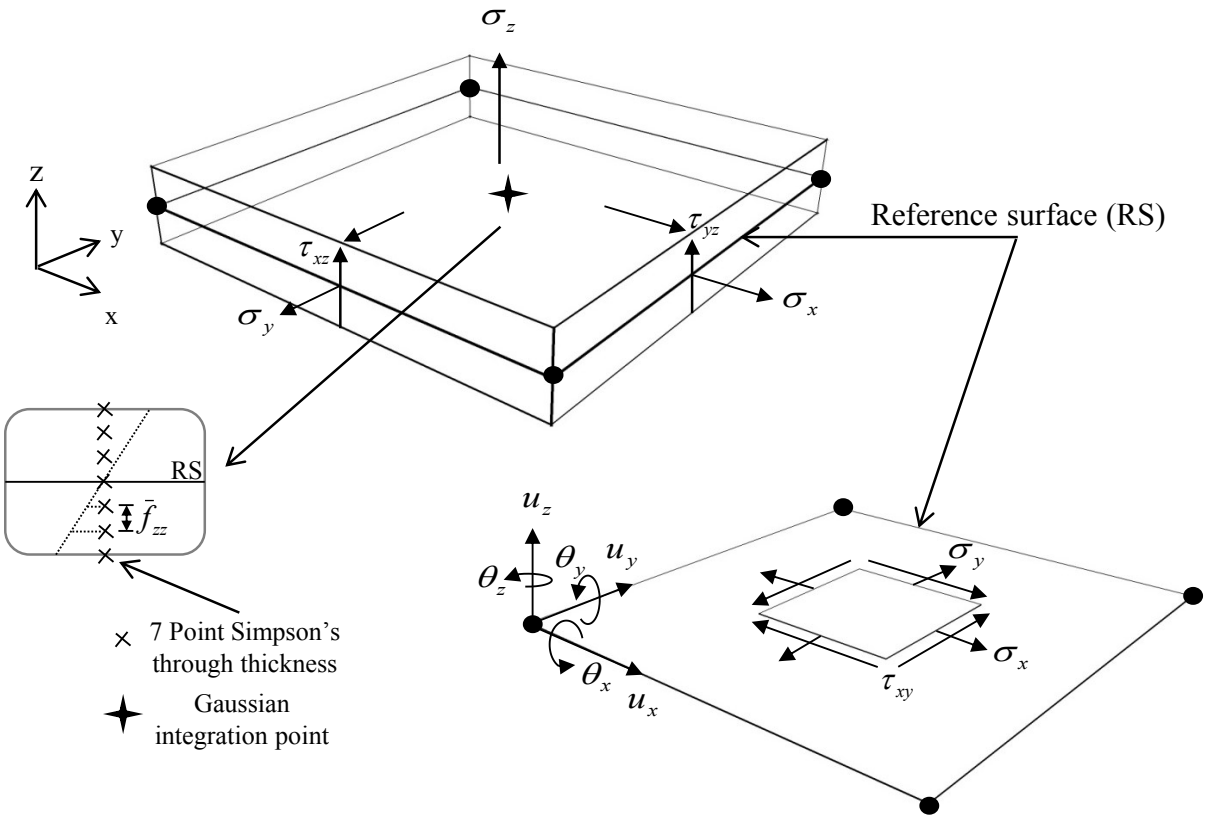

Fig. 2 Homogeneous shell element with five stress components

2.1 Stability of the Explicit Formulation

The explicit algorithm uses the central-difference operator for integration of the equations of motion, shown in (8) and iterates without formation and inversion of the mass and stiffness

matrices. Thus the reduced integration explicit formulation provides a computationally inexpensive solution compared to the fully integrated implicit procedure. The central-difference operator of the explicit procedure is conditionally stable, thus requires shorter time step size for mesh with small elements or larger wave speed.

$$[M]\{\ddot{u}\}+[U]-[W]=0 \tag{8}$$

where, u^n is the displacement degree of freedom. The mass matrix $[M]$ is calculated as (9) in which ρ_{i0} is the i^{th} element reference density, n is the number of degrees of freedom, $[N]$ is the shape function and V represents volume of the element. The internal energy $[U]$ and external work done $[W]$ are estimated as (10) and (11), respectively.

$$[M]=\sum_{i=1}^{n}\int_{V_0}\rho_{i0}\left[N_i^T\right][N_i]dV_{i0} \tag{9}$$

$$[U]=\sum_{i=1}^{n}\int_{S}\left[B_i^T\right]\{\sigma_i\}dV_{i0} \tag{10}$$

$$[W]=\sum_{i=1}^{n}\int_{S}\left[N_i^T\right]\{t_i\}dS_i+\int_{V}\left[N_i^T\right]\{f_i\}dV_i \tag{11}$$

The parameters σ, t and f represents stress, external traction and body force vectors, respectively. $[B]$ is the strain-deformation transformation matrix; S denote the surface of finite body and V_0 the initial volume.

The explicit analysis procedure implements the system of equation shown in (8) together with diagonal element mass matrices. The equations of motion for the body are integrated using the explicit central difference integration rule [21].

$$\dot{u}^n_{\left(j+\frac{1}{2}\right)}=\dot{u}^n_{\left(j-\frac{1}{2}\right)}+\frac{\Delta t_{(j+1)}+\Delta t_{(j)}}{2}\ddot{u}^n_{(j)} \tag{12}$$

$$u^n_{(j+1)}=u^n_{(j)}+\Delta t_{(j+1)}\dot{u}^n_{\left(j+\frac{1}{2}\right)} \tag{13}$$

where, $\dot{u}^n$ and $\ddot{u}^n$ are the velocity and acceleration degrees of freedom, respectively. The subscript (j) refers to increment number and $\left(j-\frac{1}{2}\right)$, $\left(j+\frac{1}{2}\right)$ refers to mid increment values. The central difference integration operator is explicit in the sense that the kinetic state is advanced using known values of $\dot{u}^n_{\left(j-\frac{1}{2}\right)}$ and $\ddot{u}^n_j$ from previous increment. The explicit integration rule is quite simple, although its computational efficiency is achieved through the use of diagonal element mass matrices, vital in computation of the initial accelerations as shown in (14).

$$\left\{\ddot{u}^n_j\right\} = \left[M\right]^{-1}\left[W_j - U_j\right] \tag{14}$$

Explicit analysis is conditionally stable; there are many approaches to achieve conditional stability. In this research, the time step approach in which the time increment is related to the membrane response of the element has been employed. A time increment is said to be stable when the inverse of the highest frequency of the elements and the highest frequency associated with the transverse shear response do not exceed the inverse of the highest frequency associated with the membrane response of the structure.

Rotary inertia for transverse shear response is proportional to the cube of the thickness, which also represents the mass of the system. Membrane stiffness, mass associated with membrane deformation, and transverse shear stiffness of the element are proportional to the thickness. As the thickness of the element reduces, the frequencies associated with transverse shear increases proportional to the inverse of the thickness, while the membrane frequencies remain constant. Hence, without scaling, the time step would reduce significantly as the thickness reduces. For the S4R element, a non-dimensional rotary inertia scaling (R) is introduced to keep the rotary inertia within a fixed fraction $\left({L_c}^2 \big/ h^2\right)$ of the mass contribution, where, L_c, h represents the characteristics length of element and thickness, accordingly.

Thickness change of the element depends on the effective section Poisons ratio (ν). Based on the basic assumption for shell that the normal stress normal to the thickness of shell is non-resistant $(\sigma_z = 0)$, the linear elasticity strain along the thickness direction can be written as (15),

$$\varepsilon_z = -\frac{\nu}{1-\nu}\left(\varepsilon_{xx} + \varepsilon_{yy}\right) \tag{15}$$

Hence, the logarithmic strain along the thickness direction is shown in (16),

$$\ln\left(\frac{h}{h_o}\right) = -\frac{\nu}{1-\nu}\left(\ln\left(\frac{l_x}{l_x^0}\right) + \ln\left(\frac{l_y}{l_y^0}\right)\right) \tag{16}$$

Equation (16) is further simplified in (17), that represents the thickness change of the element, where A_o is the initial reference surface area.

$$\frac{h}{h_o} = \left(\frac{A}{A_o}\right)^{-\frac{\nu}{1-\nu}} \tag{17}$$

Rotary inertia of the element must be higher than the rotational inertia of the mass at the nodes rotating about an axis through the centre of the element.

Bulk viscosity (commonly known as the second or expansion viscosity) is a measure of the resistance to volume change. It is used to improve the stability of the simulation. For the displacement degrees of freedom, linear bulk viscosity introduces damping associated with volumetric straining. It is used to avoid unwanted noise in the solution or spurious overshoot in the response amplitude. The linear bulk viscosity pressure ρ_{bv} associated with the volumetric strain rate is shown in (18). The high frequency ringing in shell elements is damped in the rotational degrees of freedom with the linear bulk viscosity acting on the mean curvature strain rate. The bulk viscosity pressure m, introduced by the damped rotational degrees of freedom is shown in (19).

$$\rho_{bv} = b\rho c_d L_c \Delta\varepsilon_{vol} \tag{18}$$

$$m = b\frac{h_0^2}{12}\rho c_d L_c \frac{\Delta\kappa}{\Delta t} \tag{19}$$

Parameters $b, \rho, c_d, h_o, L_c, \Delta\varepsilon_{vol}$ represent damping coefficient (default value 0.06), mass density, current dilatational wave speed, initial thickness, characteristics length and volumetric strain rate, respectively. $\Delta\kappa/\Delta t$, represents twice the mean curvature strain rate,

where, $\Delta\kappa_{xy} = \Delta\kappa_{xx} + \Delta\kappa_{yy}$. The dilatational wave speed (c_d) is given in terms of the effective Lamé's constants λ' and μ' in (20). The stability limit of the explicit solution is expressed as $\Delta t = \min\left(L_c / c_d\right)$. The resultant pressure moment (mh), adds to the direct components of moment resultant, where h is the changed thickness, derived from (17).

$$c_d = \sqrt{\frac{(\lambda' + 2\mu')}{\rho}} \tag{20}$$

2.2 Transverse Shear Stiffness

For finite-strain shell elements, the transverse shear stiffness is defined such that it matches with that of a three-dimensional solid for the case of bending about x-axis. The transverse shear stiffness for shell elements is calculated as shown in (21), where $\overline{K}_{xy}$ represents the components of the section shear stiffness. The dimensionless factor f_p is calculated as shown in (22).

$$\overline{K}_{xy} = f_p K^{ts}_{xy} \tag{21}$$

$$f_p = 1 \Big/ \left(1 + 0.25 \times 10^{-4} \frac{A}{h^2}\right) \tag{22}$$

The transverse shear stiffness is idealised as the initial, linear elastic stiffness of the shell in response to the pure transverse shear strains. Transverse shear stiffness for homogeneous elements made of a linear, orthotropic elastic material, where the strong material direction aligns with the element's local x-direction is given by (23), where G_{xz} and G_{yz} are the material's shear moduli in the out-of-plane direction, and the constant $\left(5/6\right)$ represents the shear correction coefficient that matches the transverse shear energy of the shell to a three-dimensional structure in pure bending.

$$K^{ts}_{xx} = \frac{5}{6} G_{xz} h, \quad K^{ts}_{yy} = \frac{5}{6} G_{yz} h, \quad K^{ts}_{xy} = 0.0 \tag{23}$$

2.3 Constitutive Relation and Stabilisation

The relation of the curvilinear components of resultant transverse shear forces $[Q]$ to transverse shear strains $\bar{\gamma}^{ts}$ and the transverse shear stiffness in curvilinear coordinate $[C_s]$ is expressed using the St. Venant-Kirchhoff constitutive model (24),

$$\begin{Bmatrix} Q^x \\ Q^y \end{Bmatrix} = [C_s] \begin{Bmatrix} \bar{\gamma}_x^{ts} \\ \bar{\gamma}_y^{ts} \end{Bmatrix} \tag{24}$$

$$[C_s] = \frac{5}{6} G_s h \begin{bmatrix} A^{xx} & A^{xy} \\ A^{yx} & A^{yy} \end{bmatrix} \tag{25}$$

The curvilinear component of transverse shear stiffness for a single isotropic layer of S4R element is expressed in (25), where, the matrix $[A^{xy}]$ is the inverse of matrix $[A_{xy}]$. The components of A_{xy} is given as the product of reference surface position vector. The Cauchy or true transverse shear force components in the shell orthonormal coordinate system $\{q^x, q^y\}^T$ are calculated with the coordinate transformation as (26), where A is the reference surface area of the element and a is its current area.

$$[q] = \begin{Bmatrix} q^x \\ q^y \end{Bmatrix} = \frac{A}{a} \begin{bmatrix} f_x^x & f_y^x \\ f_x^y & f_y^y \end{bmatrix} \begin{Bmatrix} Q^x \\ Q^y \end{Bmatrix} \tag{26}$$

An assumed strain method based on the Hu-Washizu principle has been adopted to avoid shear-locking, which typically arises as the thickness of the element reduces. The assumed transverse shear strain field $\bar{\gamma}_x^{ts}, \bar{\gamma}_y^{ts}$ is shown in (27), where, $\gamma_x^E, \gamma_x^F, \gamma_y^G, \gamma_y^H$ are the covariant transverse shear strains at mid-points of element boundaries.

$$\begin{aligned} \bar{\gamma}_x^{ts} &= \frac{1}{2}\left[(1-\alpha)\gamma_x^F + (1+\alpha)\gamma_x^H\right] \\ \bar{\gamma}_y^{ts} &= \frac{1}{2}\left[(1-\beta)\gamma_y^E + (1+\beta)\gamma_y^G\right] \end{aligned} \tag{27}$$

For reduced-integration S4R elements, the transverse shear force components are evaluated at the center of the element. The transverse shear strain of the homogeneous part at the center of the element $(\bar{\gamma}_0^{ts})$ and the hourglass transverse shear strain vector (γ_{hg}) are defined by (28),

where, γ_{bf}, γ_{cc} represent strains associated with 'butterfly' deformation pattern and 'crop circle' deformation pattern, respectively.

$$\bar{\gamma}_0^{ts} = \frac{1}{2}\begin{Bmatrix}\gamma_x^F + \gamma_x^H \\ \gamma_y^E + \gamma_y^G\end{Bmatrix} + \gamma_{cc}\begin{Bmatrix}c_\alpha \\ c_\beta\end{Bmatrix} \text{ and } \gamma_{hg} = \begin{Bmatrix}\gamma_{bf} \\ \gamma_{cc}\end{Bmatrix} \tag{28}$$

The crop circle pattern γ_{cc}, suitable for relax hourglass stiffness control, corresponds to a deformation pattern that resembles the sweeping over the element normal in a circular pattern. It is idealised by zero vertical deflection at the nodes and a nodal rotation vector pattern. The advantages of introducing the crop circle pattern in the homogeneous part of the transverse shear strain is, the element's response becomes independent of the choice of node numbering. Furthermore, for explicit dynamic analyses the element distortion coefficients c_α, c_β are chosen to minimise the highest frequencies associated with the homogeneous part of the transverse shear response, thus control the influence of element distortion on the stable time increment and stabilises the explicit algorithm.

4. Calibration of the Masonry Material in the Explicit Shell Formulation

The material properties for masonry have been calibrated using an experimental dataset taken from a full scale 4m long × 2.5m high unreinforced masonry wall (Fig. 3) reported in [22].

Fig. 3 Wall Configurations (redrawn from [22])

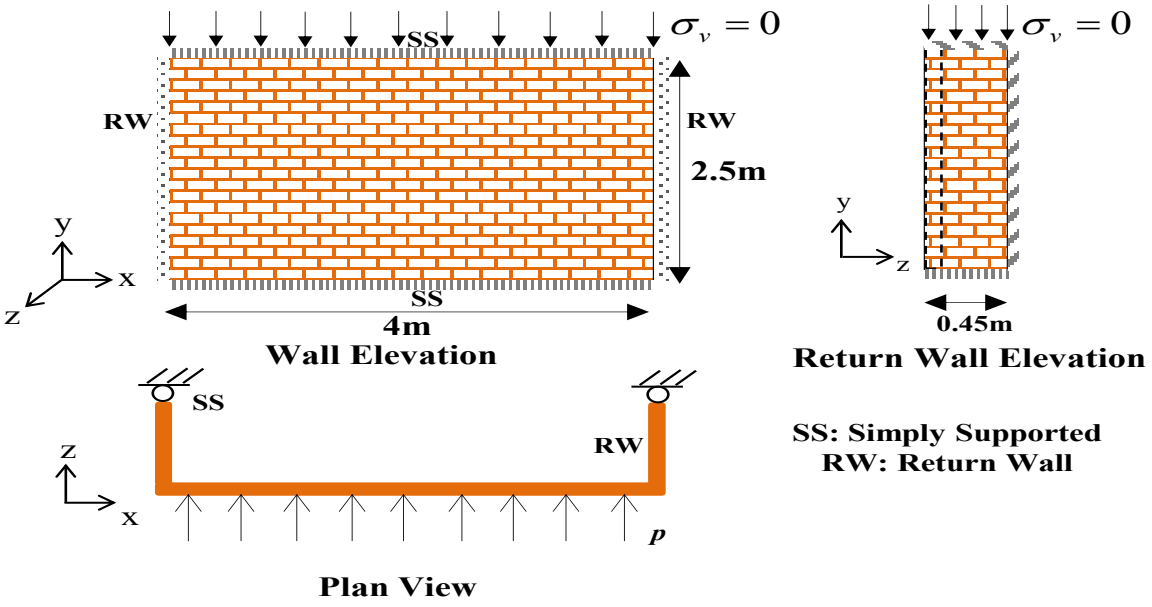

4.1 Description of the Experiment

The "C" shaped wall was subject to uniformly distributed lateral pressure loading normal to its web surface whilst the faces of the two flanges remained unloaded as shown in Fig. 3. The wall was made of solid 10 hole-cored clay bricks of $230mm$ long × $76mm$ high × $110mm$ thick and $10mm$ thick M3 (1:1:6 cement : lime : sand) mortar joints and tested at the University of Adelaide as reported in [22]. In this study, the load-displacement response and the mode of failure of the wall were used for the calibration.

The wall was simply supported along the top and the bottom edges; $0.45m$ long return walls were constructed along the vertical edges of the main wall to provide some moment restraint. The vertical ends of the return walls were clamped by channel sections that restrained its lateral movements. Uniform surface pressure load was applied with an air bag placed between the outer face of the web of the "C" wall and a reaction frame. The reaction forces were recorded using load cells embedded within the reaction frame; the total reaction was divided by the surface area of the wall to calculate the applied surface pressure using equilibrium equations; this approach was used as it could not be ascertained that the whole of the airbag surface was fully in contact with the loading surface (and hence the air pressure measured in the air bag was not used in the pressure–displacement characterisation of the wall). To be consistent with this experimental procedure, the reaction forces in the wall boundary obtained from the EFE analysis was divided by the surface area of the loaded web to obtain a measure of the surface pressure at each load step. The mid-span out-of-plane displacement was used in the definition of the load (or, pressure)–displacement response characteristics of the wall. Furthermore, the failure modes were checked with the contour plots of the logarithmic principal strains.

4.2 EFE Modelling

The wall shown in Fig. 3 was modelled using the four-noded reduced integration S4R shell elements with seven-point Simpson's integration through the thickness of the elements. Thickness of all wall parts was set as 110 mm consistent with the experiment. There were 861 elements, 968 nodes and 5808 degrees of freedom in the model. To simulate masonry behaviour appropriately, careful meshing involving units and mortar layers is essential; some authors have used random meshing involving non-quadratic elements [16, 23], in this research such randomness was avoided. A mesh convergence study was conducted, to obtain the optimum mesh size that ensures accuracy of the analysis whilst being computationally economical. Convergence for both the in-plane and the out-of-plane loads was investigated

and a square mesh size of 120 mm, consisting some parts of the brick and bed and perpend joints, was selected to represent masonry.

The bottom of the wall was restrained translationally in all three directions. Top boundary condition was selected such that it allowed the application of compression load in the vertical direction (as shown in Fig. 3) and provided translational restrain in the other two lateral directions (u_x, u_z). Vertical edges of the return walls were translationally restrained (u_z) along the z-direction. Top and bottom of return walls were supported to provide the out-of-plane restrain only (u_x) and both out-of-plane and vertical pre-compression restrain (u_x, u_y), respectively. A monotonically increasing uniform surface pressure load p was applied along the out-of-plane direction (z) of wall as shown in Fig. 3.

The calibrated material parameters for the unreinforced masonry are presented in Table 1.

Table.1: Material properties for URM

Item	Parameters	Values	Notes	Item	Parameters	Values	Notes
1	$f_{tp}(MPa)$	0.4	[22]	11	β	-1	[1]
2	$G_{ftp}(Nmm/mm^2)$	3.0	Assumed	12	γ	4	[20]
3	$f_{tn}(MPa)$	0.19	f_{tp}/f_{tn} ratio	13	ε_p	0.0005	[20]
4	$G_{ftn}(Nmm/mm^2)$	0.5	Assumed	14	$L_c(mm)$	125	Assumed
5	α	1.1	[20]	15	$E_p(MPa)$	2000	Assumed
6	α_g	1	[1]	16	$E_n(MPa)$	3500	[22]
7	$f_{cp}(MPa)$	5	f_{cp}/f_{cn} ratio	17	$E_z(MPa)$	3500	Assumed
8	$G_{fcp}(Nmm/mm^2)$	0.003	Assumed	18	ν_p	0.2	[1]
9	$f_{cn}(MPa)$	11	[22]	19	ν_n	0.2	[1]
10	$G_{fcn}(Nmm/mm^2)$	10	[20]	20	ν_z	0.2	[20]
				21	$G(MPa)$	2800	Calculated

Material property of specimens addressed in [22] showed different tensile and compressive strengths and modulus of elasticity of masonry for the set of walls tested. Although same batch of bricks and mortar composition were used in the construction, the flexural tensile bond strength was found to vary significantly compared to other properties due to its sensitivity to workmanship and handling. Therefore, average of all other properties was considered representative in the modelling, whilst taking the tensile bond strength reported for each wall as given in the dataset. These properties were calibrated using trial and error method until the predicted pressure-displacement characteristics and the failure mode matched well with the reported information. In addition to these material datasets, initial transverse shear stiffness and the number of integration points through the thickness of the shell element have also been defined.

4.3 Results: Global Response of the Wall

The material properties presented in Section 4.1.4 were so chosen that the EFE model predicted both the load – displacement response and the mode of failure of the wall in close proximity with the experimental results reported. The moment–curvature relationship obtained from the model was also compared with the analytical expression given in [10].

4.3.1 Load-Displacement Relation

Fig. 4 (a) shows comparison between the experimental and calculated load-displacement responses from the EFE model for the wall. The deflected shape of wall is shown in Fig. 4 (b).

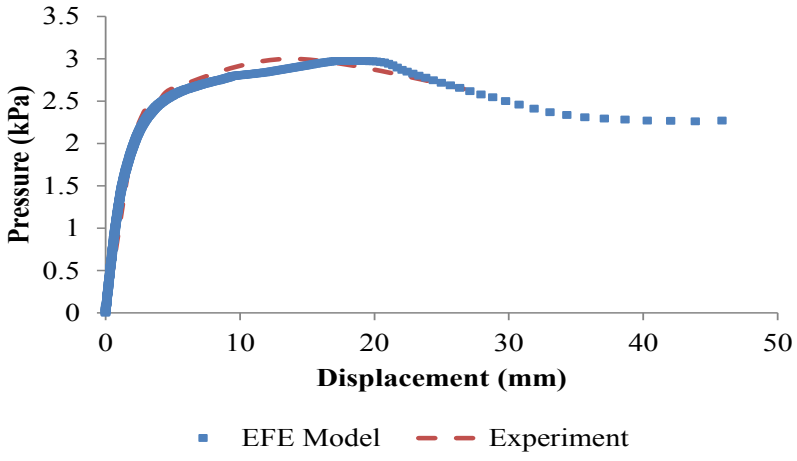

(a)

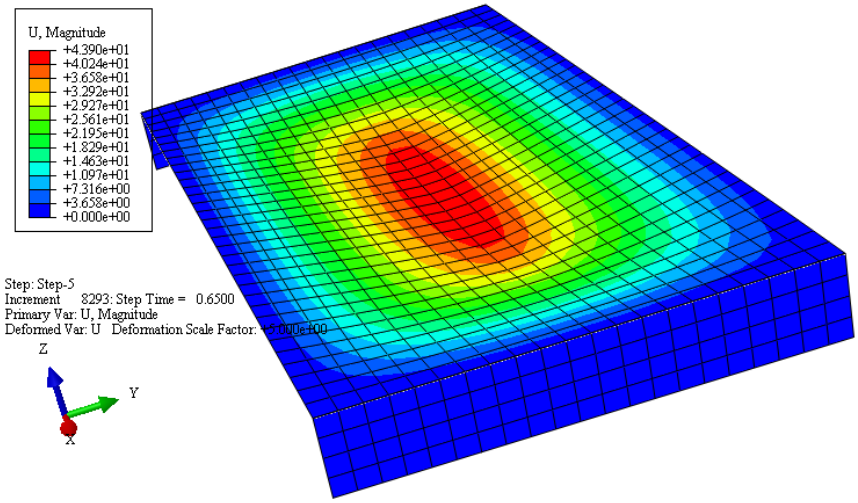

(b)

Fig. 4 Out-of-plane response of the wall (a) Load-displacement diagram, (b) Deflected Shape

The experiment and the EFE model results show that the wall reached a peak out-of-plane pressure of 3.04 kPa and 2.97 kPa, respectively (an error of just 2.3%, which is considered quite reasonable). Within the elastic range (at a mid-span displacement of 3 mm), surface pressure observed from the experiment and the FE model were 2.41 kPa and 2.28 kPa, respectively; while in the inelastic range (at a mid-span displacement of 14 mm), the surface pressures were 3.0 kPa and 2.9 kPa, respectively. The close agreement in the hardening and the softening regime of the load-displacement responses ensures the appropriateness of the calibrated material parameters for the VUMAT model.

4.3.2 Mode of Failure

The mode of failure of the wall reported in [22] is schematically shown in Fig. 5 (a); a two-way flexural cracking pattern comprising of horizontal cracking at mid height and stepped diagonal cracking to all four corners of the wall can be seen in the figure. The logarithmic strain contour on the unloaded (tension) face of the wall is shown in Fig. 5 (b). The maximum principal logarithmic strain plot shows, localisation of strain (0.0042) along the mid-span that confirms the crack formation in the zone. A profound diagonal strain distribution pattern (strain of 0.0025) is observed from mid-span towards the edges of the return walls, identical to the failure mode observed in the experiment. The predicted crack path is thus considered matching appropriately with the experimental failure mode.

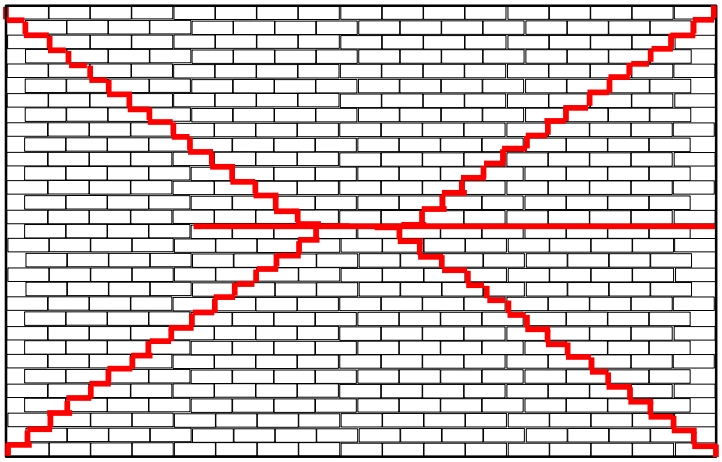

(a)

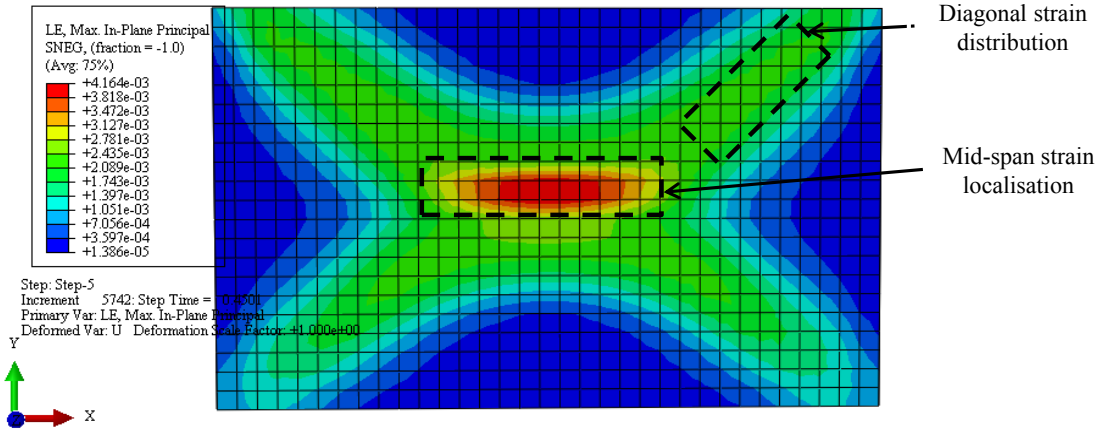

(b)

Fig. 5 Mode of failure (a) Experiment (redrawn from [22]), (b) EFE Model

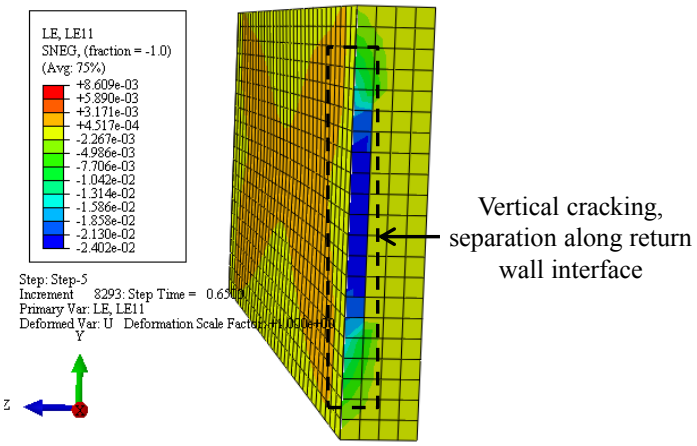

Fig. 6 Separation at Return Wall

Strain plots parallel to bed joint direction [shown in Fig. 6], shows vertical crack formation along the return wall where the logarithmic strain reaches 0.024, causing split of joint between the out-of-plane wall and return wall.

4.3.3 Moment-Curvature Relation

Moment - curvature $(\overline{M}-\varphi)$ relationship for the out-of-plane loaded wall is established to enable predicting the flexural stiffness and infer the (pseudo) ductility of the unreinforced masonry walls. The section moments and corresponding curvature is calculated from the EFE model and are shown in Fig. 7. Element with the maximum section curvature at mid-span was selected to establish the $(\overline{M}-\varphi)$ relationship.

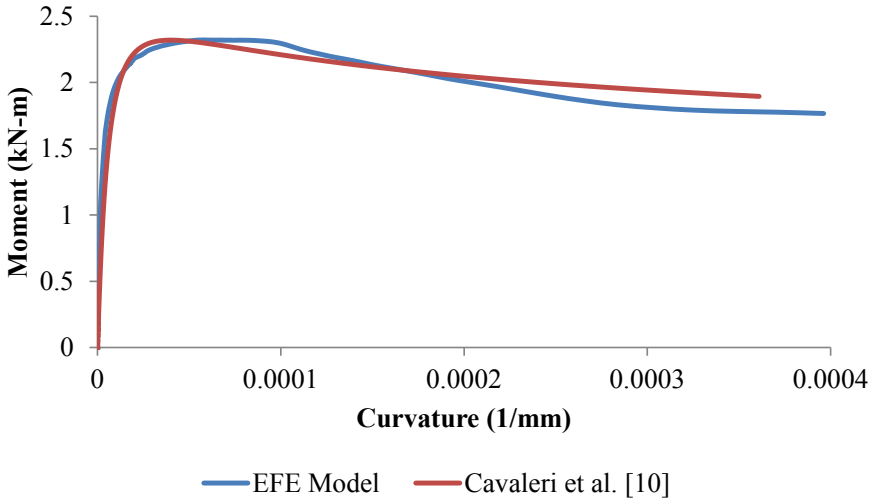

Fig. 7 Moment-Curvature Relation

Maximum section moment of the element and its corresponding curvature were 2.3 kN-m and $5\times10^{-5}\,(1/mm)$, respectively. A sudden increase in curvature was observed beyond peak moment at the critical section where the relationship was observed which demonstrated the unstable out-of plane deformation of the wall. The maximum curvature of the section was $4\times10^{-4}\,(1/mm)$. The proposed $(\overline{M}-\varphi)$ relationship for masonry by [10], shown in (29), was used to compare with the $(\overline{M}-\varphi)$ relation obtained from the EFE model.

$$\tilde{m}=\tilde{m}_{\max}\frac{r\left(\tilde{\phi}/\tilde{\varphi}_0\right)}{r-1+\left(\tilde{\phi}/\tilde{\varphi}_0\right)^r}\quad\text{for}\quad 0\le\tilde{\varphi}\le 1.5\tilde{\varphi}_0 \tag{29}$$

where, $\tilde{m}$ and $\tilde{\varphi}_0$ represent normalised moment and curvature at maximum moment of the section, respectively. The proposed relationship (29) was used to determine the shape of the $(\overline{M}-\varphi)$ curve corresponding to a curvature representing 1.5 times of the maximum moment capacity of the section $\tilde{\varphi}_0$. The post-peak part in this construction was assumed to follow the natural slope of $\tilde{\varphi}_0 - 1.5\tilde{\varphi}_0$ region. Parameter r defines the shape of $(\overline{M}-\varphi)$ curve; in this case a higher magnitude 1.15 was assigned for the comparatively low tensile strength material. The $(\overline{M}-\varphi)$ relationship from the EFE model and the analytical expression matched well; which confirms the accuracy of the obtained $(\overline{M}-\varphi)$ relationship.

4.4 Results: Local Response of the Wall

The local stress- strain relation at two locations of the wall viz., mid-span and top right diagonal are reported in Fig. 8.

Fig. 8 (a) shows the stress-strain plot along parallel and normal to bed joint at the mid-span of the wall. Elements in the region experienced a maximum tensile stress of 0.19 MPa along the normal to bed joint direction, equal to the specified tensile strength. The maximum parallel stress 0.17 MPa is, however, lower than its specified strength input of 0.4MPa; this shows that the masonry in the parallel direction has ability to resist additional stresses whilst the normal stress peaked. At the top right diagonal, stress-strain plot along normal and parallel to bed joint direction [Fig. 8 (b)] reveals that, the magnitude of stresses along the axes normal and parallel to the bed joint were 0.18 MPa and 0.23 MPa, respectively.

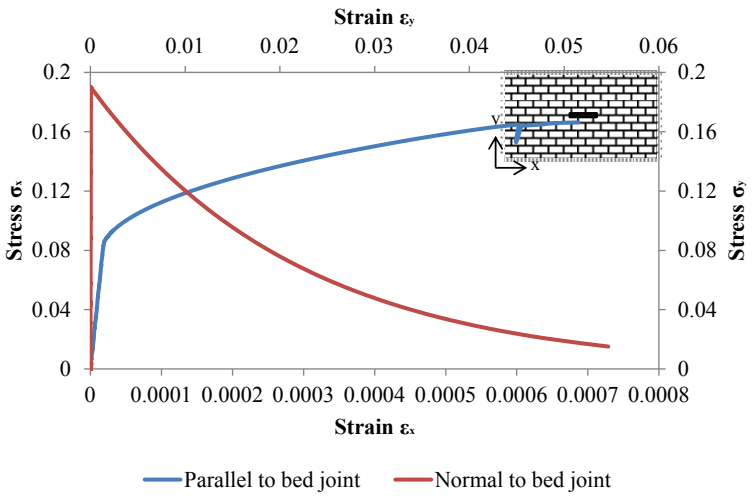

(a)

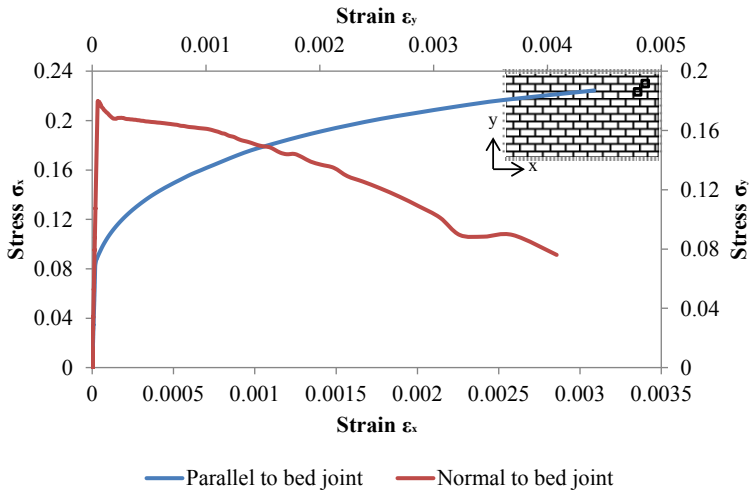

(b)

Fig. 8 Stress-strain plot (a) mid-span, (b) top right diagonal

Fig. 9 shows the strain plot parallel and normal to the bed joint directions. At wall mid-span, strain parallel to bed joint (0.0006) were much lower than strain normal to bed joint (0.055), indicating crack opening only along the normal to the bed joint direction. Furthermore, strains along the wall diagonal exceeded the cracking strain of URM in both parallel and normal to bed joint directions (0.0031 and 0.004), which confirms the formation of a stepped diagonal cracking pattern, produced due to splitting of mortar of both bed and head joints.

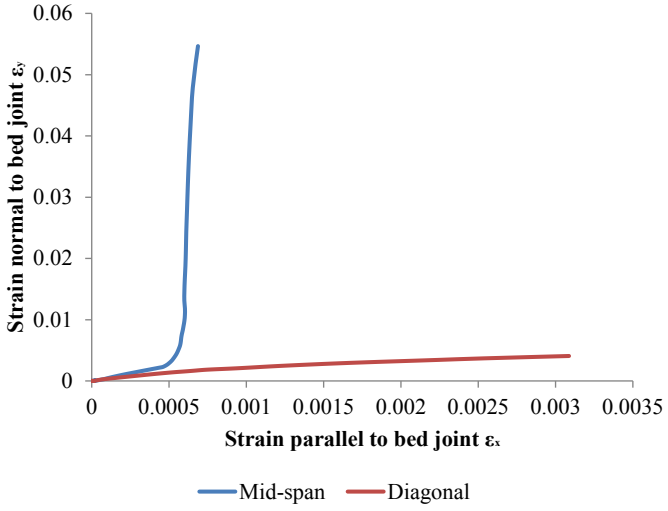

Fig. 9 Plots of strains parallel to bed joint vs normal to bed joint

Hence, the detailed analysis of the stress-strain plots confirms the crack formation along the wall mid-span and diagonals, which exhibits a true two-way out-of-plane response. During the stages of rapid strain increment (corresponding to crack formation), stress normal to bed

joint directions at the mid-span region reduced significantly compared to that of the diagonals [shown in Fig. 8 (a) and Fig. 8 (b)], which caused the drop in post-peak out-of-plane capacity.

5 Validation Using the Calibrated EFE Model

Dimension and boundary condition of walls used for validation of EFE are shown in Table. 2. A total of six walls comprising of solid walls (SS2) and walls with symmetrical opening (SO1 and SO2) and un-symmetrical opening (SO3 and SO4) were used in the validation. For reasons stated in Section 4, different flexural bond strengths f_{tp} and f_{tn} were used in the validation of all six walls, as listed in Table. 2.

Table. 2: Walls used for validation (redrawn from [22])

Panel Dimension (m)	**Wall**	σ_v **(MPa)**	**Support**			f_{tp} (MPa)	f_{tn} (MPa)
			Bottom	**Top**	**Sides**		
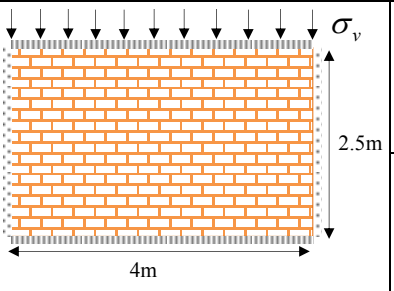	SS1	0	Simply Supported	Simply Supported	Return walls perfectly bonded	Calibrated Wall	
	SS2	0.1				0.5	0.26
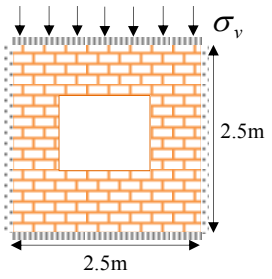	SO1	0	Simply Supported	Simply Supported	Return walls perfectly bonded	0.6	0.3
	SO2	0.1				0.6	0.3
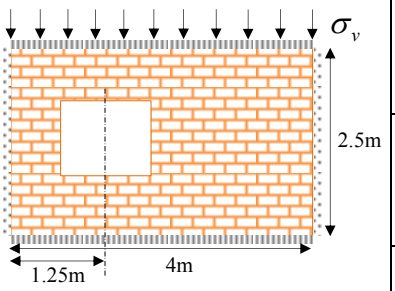	SO3	0	Simply Supported	Simply Supported	Return walls perfectly bonded	0.45	0.21
	SO4	0.05				0.45	0.21
	SO5	0		Free		0.34	0.17

The load-displacement relations and the failure modes of the analyses are shown in Table. 3. The predictions are in good agreement with the experimental results. Although failure modes from the experiments are not shown in the table for conciseness, the failure modes can be seen logical for the boundary conditions, aspect ratios and opening locations in each of the six walls reported in Table 3. The predicted ultimate loads are consistently larger than that of the experimental results; this phenomenon is important for confidently adopting the EFE model as a useful tool in practical designs.

Table. 3: Load-displacement relation and failure modes of validated walls

Wall	Load-displacement relation	Logarithmic strain plot
SS2	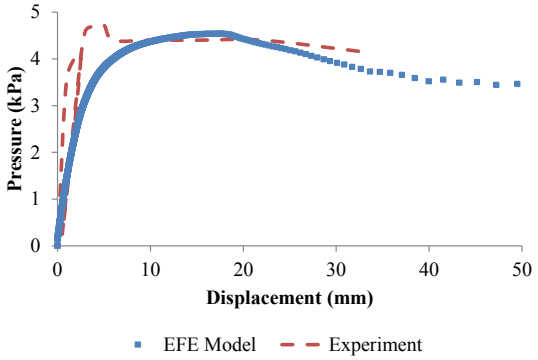	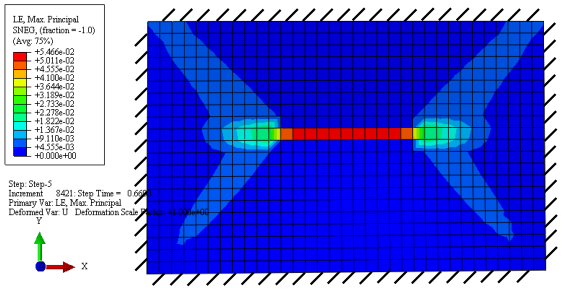
SO1	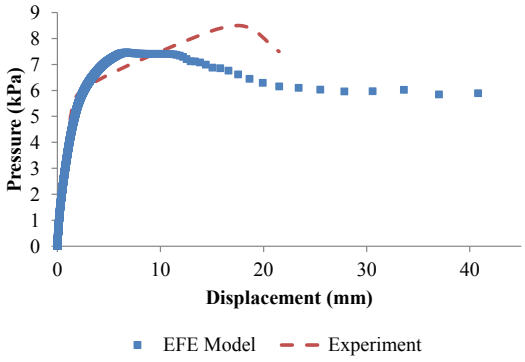	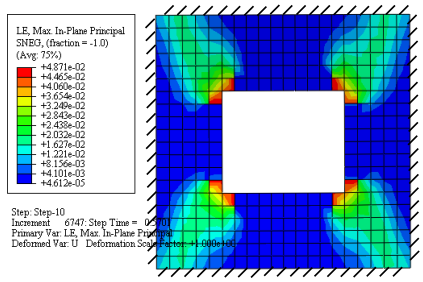
SO2	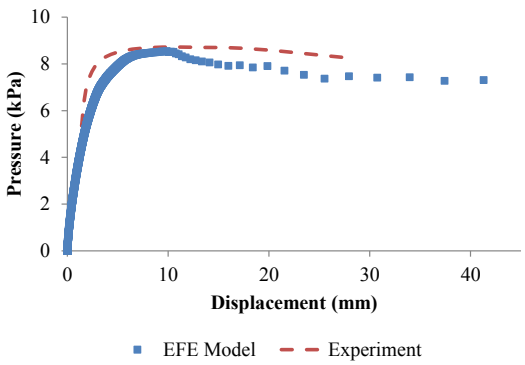	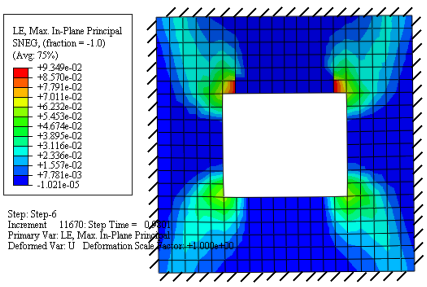

SO3	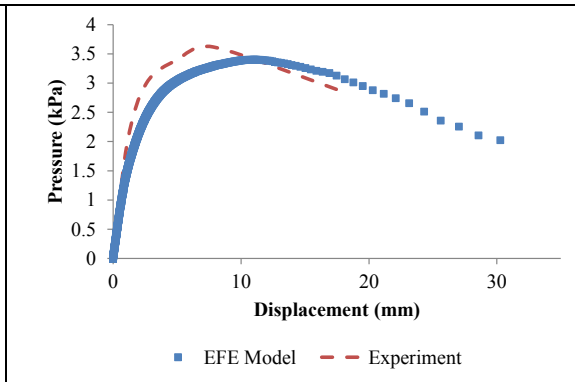	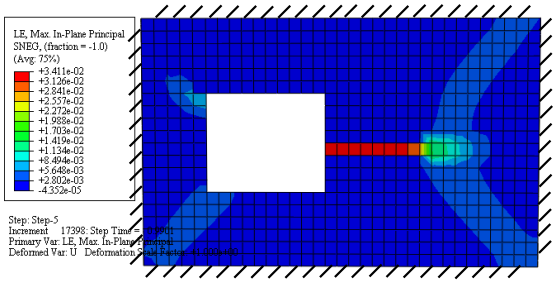
SO4	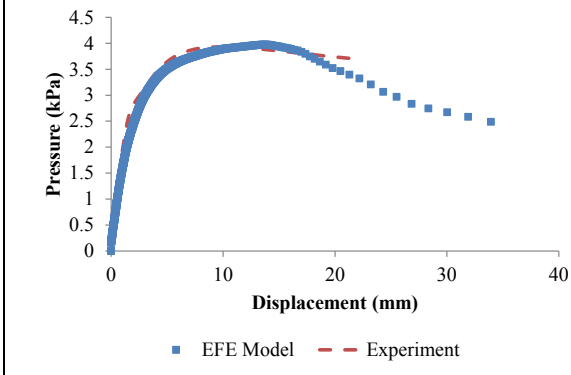	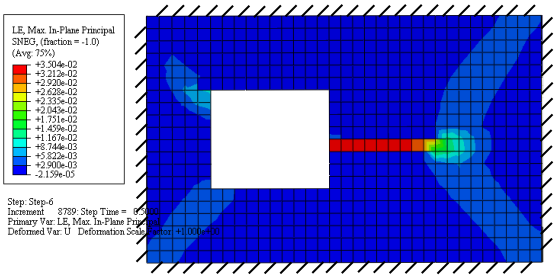
SO5	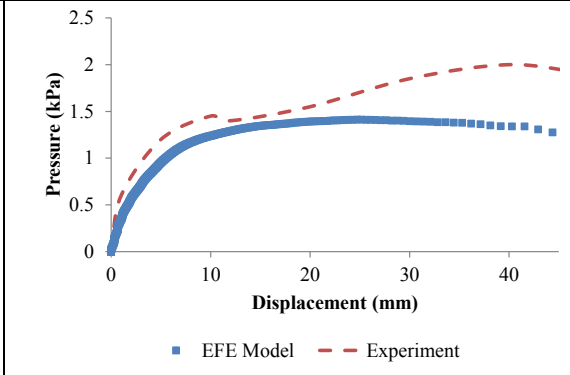	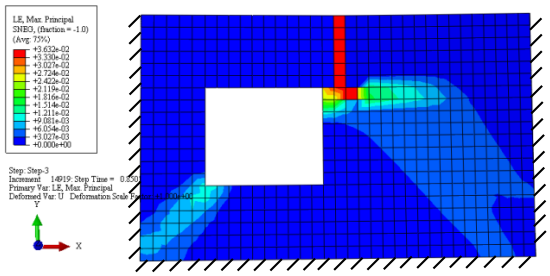

5.1 Solid Wall under Pre-compression

A vertical pre-compression of 0.1MPa was applied to the EFE model as a shell edge load in the first step of the analysis and was kept constant during the consecutive steps, until failure of the wall occurred due to the monotonically increasing uniform out-of-plane surface pressure. All input data except the flexural tensile strength [shown in Table. 2] were kept the same as that of the calibrated model. The prediction from the EFE model and the experimental observation, showed the peak capacity for wall SS2 were 4.55 MPa and 4.75 MPa, respectively (error of just 4%). The load-displacement relations from the experiment of the wall SS2 is in good agreement with the EFE model.

5.2 Walls with Symmetric Opening

Square walls SO1~SO2 with symmetric openings ($1.2m \times 1m$) were modelled. To introduce openings in solid walls, a lintel beam of S4R elements and elastic material property were assigned at the top of the openings. Wall SO2 was subjected to an additional pre-compression load of 0.1 MPa over wall SO1. The load-displacement responses of wall SO1-SO2 are shown in Table. 3; the agreement between the experimental and EFE model outcomes is quite good.

5.3 Walls with Asymmetric Opening

Rectangular walls SO3~SO5 containing an asymmetric opening ($1.2m \times 1m$) located 1250mm from the left support (as shown in Table. 2) was modelled. Wall SO4 was subjected to an additional pre-compression load of 0.05 MPa over wall SO3. Wall SO5 was constrained on three sides with only top edge unrestrained. The load-displacement responses of wall SO3~SO5 are shown in Table. 3; good agreement can be observed between the experimental and EFE model outcomes.

6 Parametric Studies

Parametric studies were conducted using the validated EFE model to improve the understanding of the out-of-plane response of URM walls under varying support conditions, aspect ratio and vertical pre-compression. A total 68 walls were analysed for this purpose. Outcomes from the parametric study are briefly discussed.

6.1 Influence of Varying Support Condition

Fig. 10 shows the calculated load-displacement diagrams for walls with varying boundary conditions. In these cases, i.e., only top and bottom simply supported (2-sides restrained), top, bottom and one vertical edge supported (3-sides restrained), all four sides simply supported (4-side) and vertical edges with return wall moment connection.

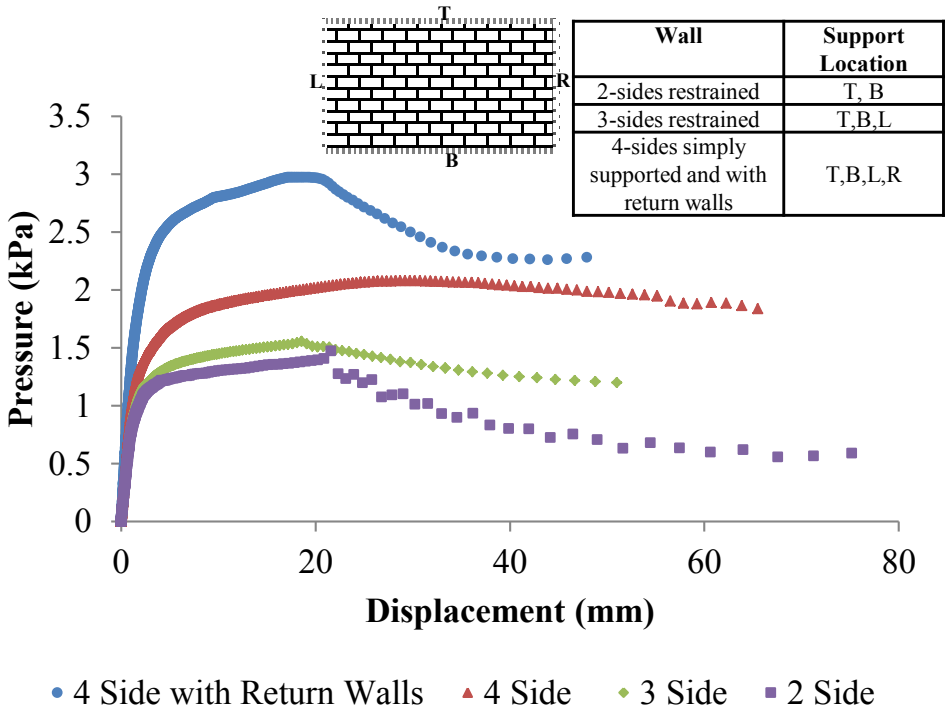

Fig. 10 Influence of support condition

As expected, the load capacity increases with more vertical supports, as these supports mobilise two-way action. The capacity of 4-side supported wall and wall with returns were 38% and 98% higher, respectively than that of the wall supported on top and bottom edges only. It is also observed that the 4-side simply supported wall showed highest ductility than the other walls. Wall with top and bottom edge supports showed the least ductility due of the absence of diagonal failure path. Fig. 11 shows the failure modes of 2-sides, 3-sides and 4-sides simply supported walls.

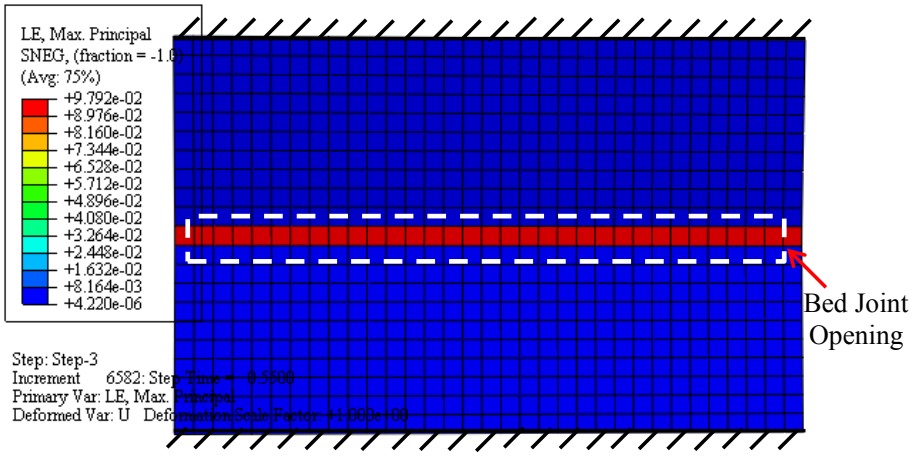

(a) 2-sides (top and bottom edges) supported

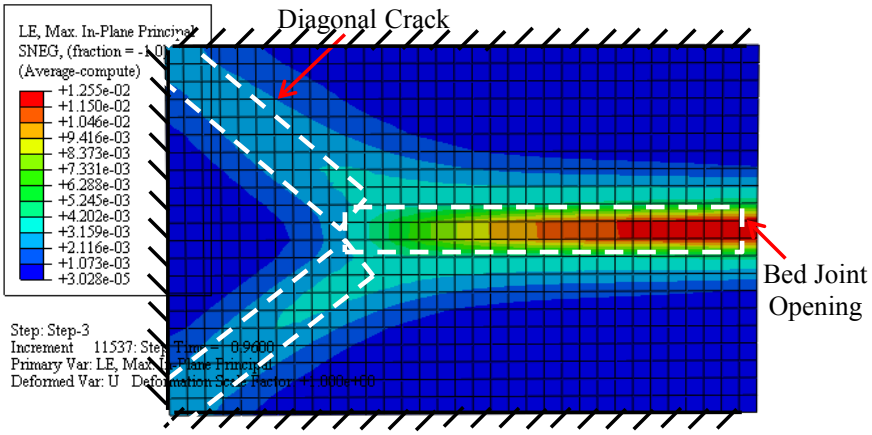

(b) 3-sides supported

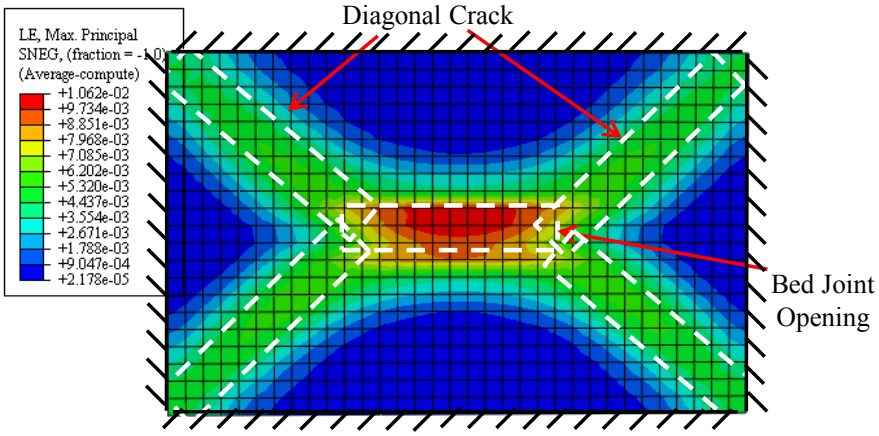

(c) 4-sides supported

Fig.11 Failure mode of walls with varying supports

6.2 Influence of Aspect Ratio

Fig. 12 shows the calculated load-displacement diagrams for walls with aspect ratios *H/L* of 0.45, 0.6, 1.0 and 1.6.

As expected, the maximum out-of-plane capacity increased significantly with the increase in H/L ratio. The taller wall (*H/L*=1.6) showed higher capacity, 67% higher than that of the square wall (*H/L*=1.0). Furthermore, the longer wall (*H/L*=0.45) showed lower capacity 50% lower than that of the square wall. Noteworthy, that the taller wall showed the least ductility than the other walls. It was also observed that ductility of the walls showed an increasing trend with decreasing *H/L* ratio. Initial stiffness of the taller and the longer walls were 12500 *N/mm* and 4000 *N/mm*, respectively. The failure modes for walls with *H/L* ratio 0.45, 1.0 and 1.6 are shown in Fig. 13.

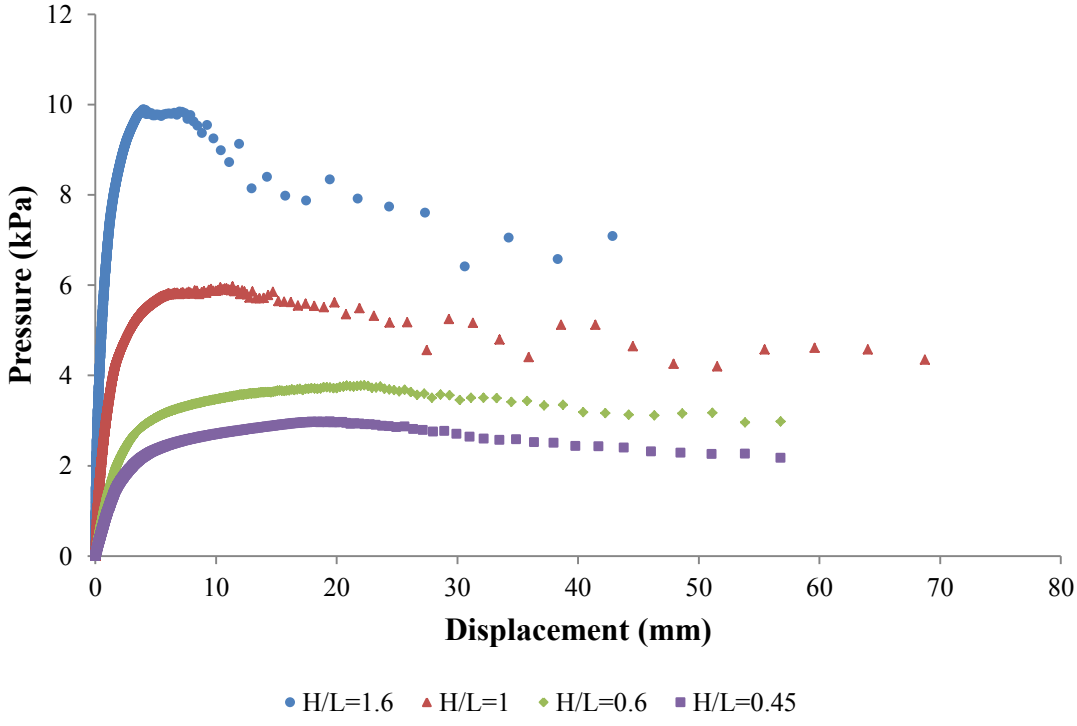

Fig. 12 Influence of aspect ratio

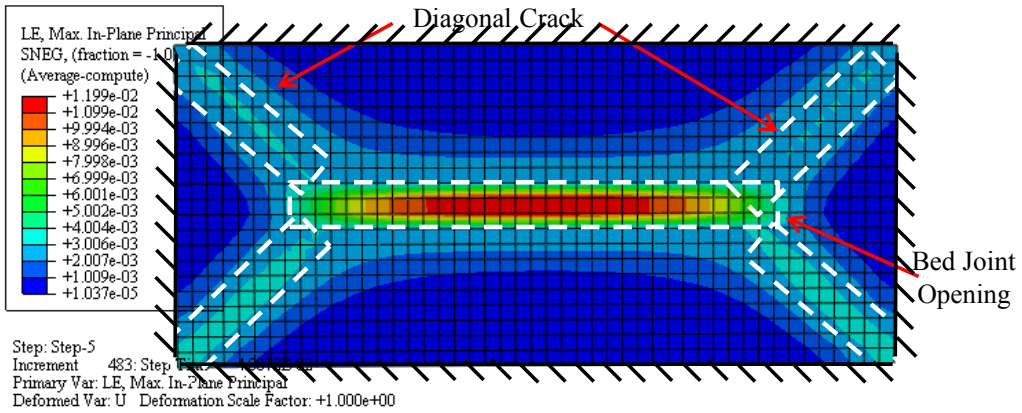

(a) H/L=0.45

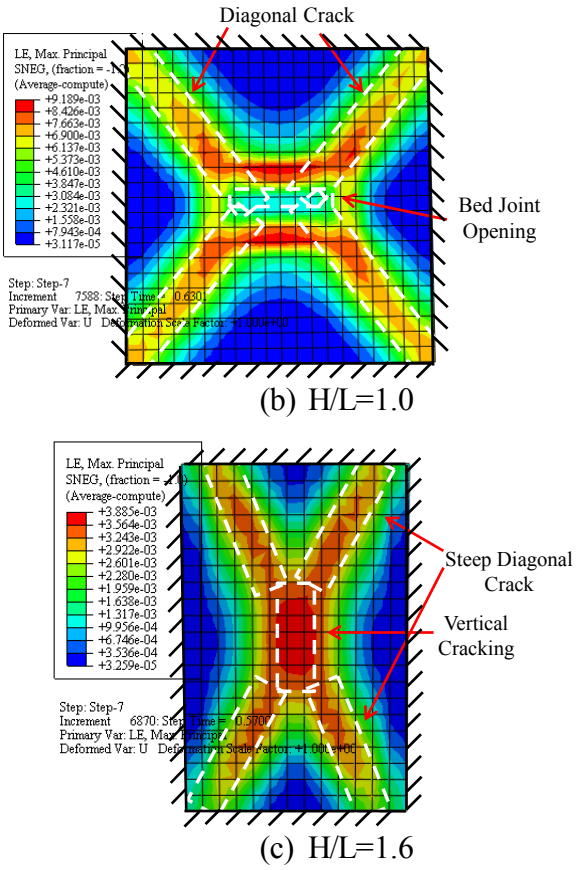

Fig.13 Failure mode of walls with varying aspect ratio

As the walls whose H/L>1.0 failed due to vertical crack passed through both bricks/blocks and vertical perpend joints higher resistance to the out-of-plane pressure resulted compared to the walls whose H/L<1.0 where the horizontal bed joint crack passed through just the weaker mortar layer.

6.3 Influence of Pre-compression

Fig. 14 shows the load-displacement relation for walls with varying vertical pre-compression loading along its top boundary. The failure modes under pre-compression of 0.5*MPa* and 5.0 *MPa* are shown in Fig. 15.

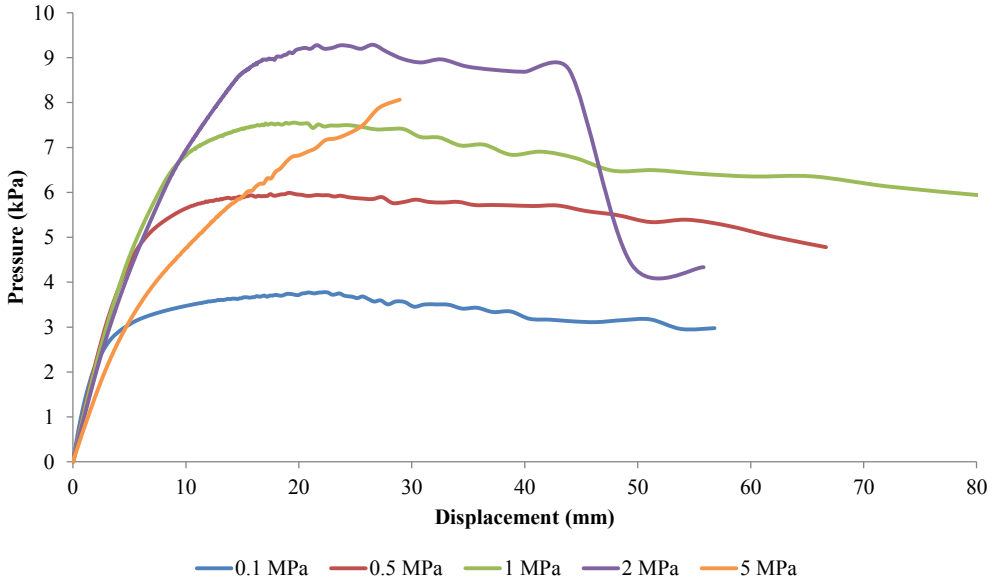

Fig. 14 Influence of pre-compression

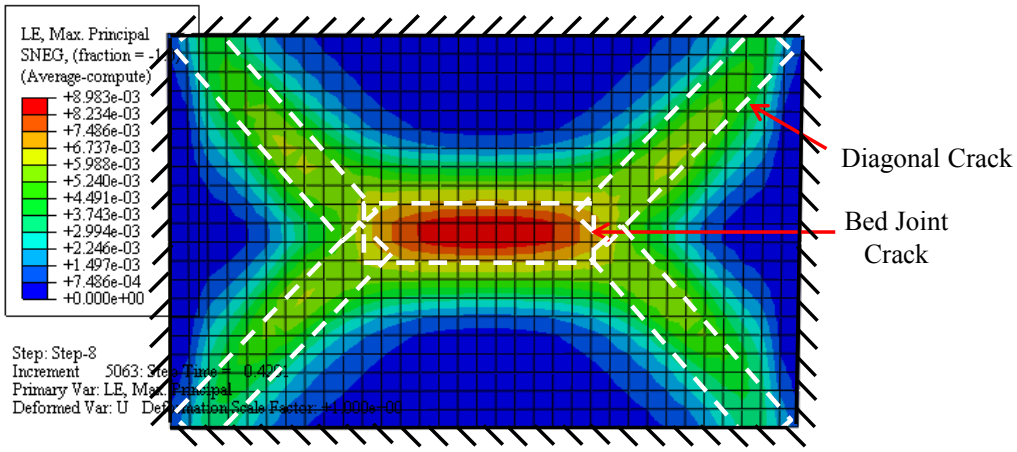

(a) 0.5 MPa

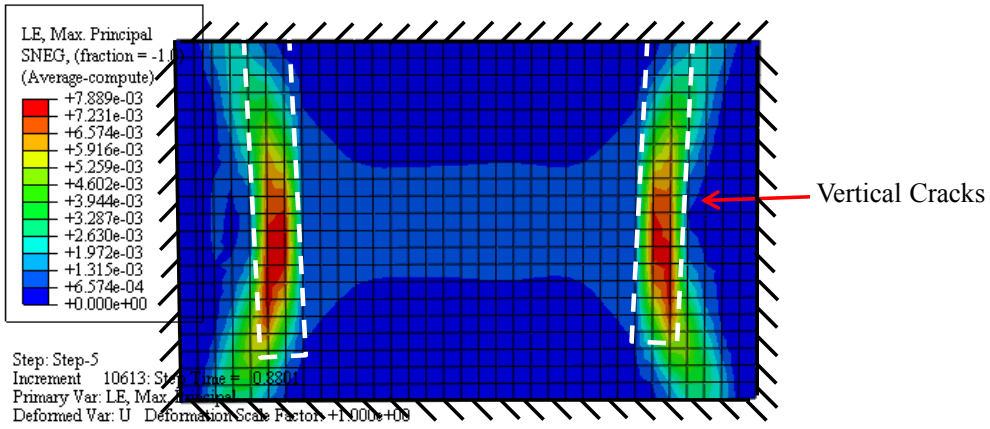

(b) 5.0 MPa

Fig. 15 Failure modes under varying pre-compression

To calculate the displacement ductility, the displacement corresponding to 80% of the ultimate out-of-plane capacity $0.8F_u$ i.e., 20% strength degradation, was considered as the ultimate displacement Δ_u [24]. Furthermore, the point of intersection between the line $0.8F_u$ and the slope of elastic stiffness was defined as the yield displacement Δ_y, as shown in Fig. 16 (a).

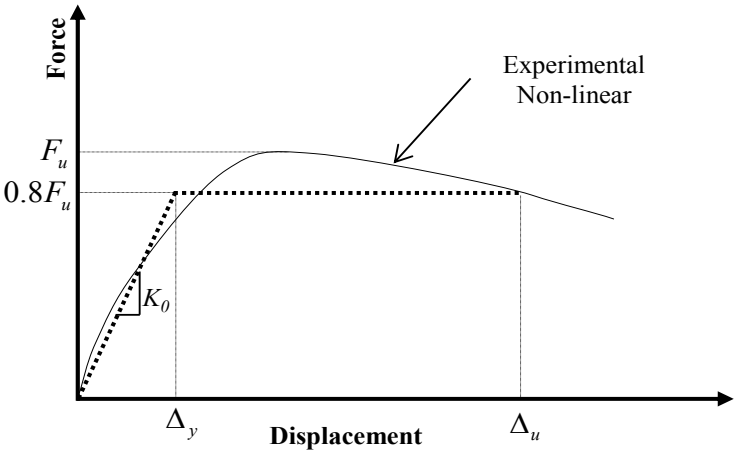

(a) Definition of Displacement Ductility

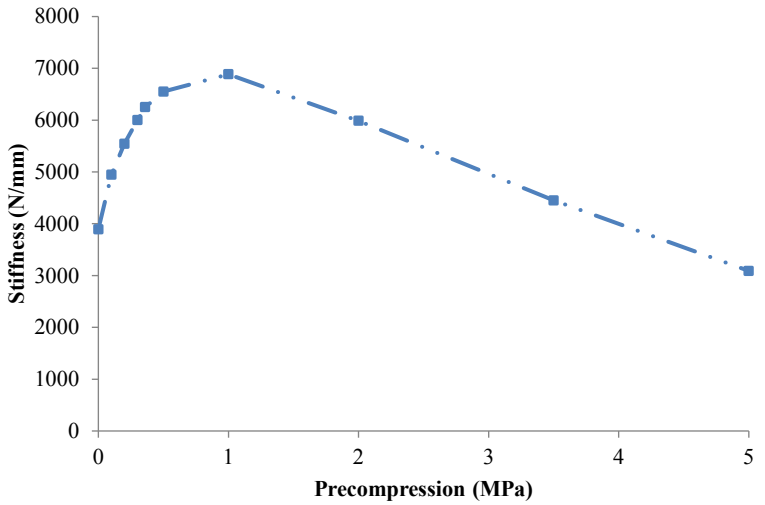

(b) Stiffness vs Pre-compression

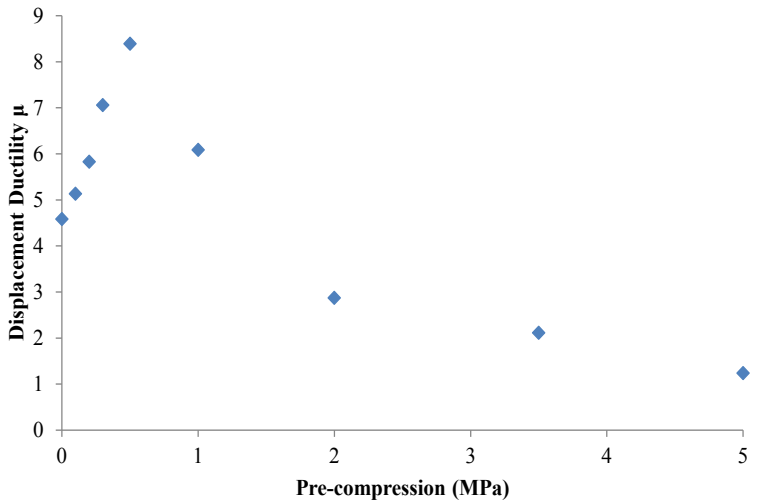

(c) Displacement Ductility vs Pre-compression

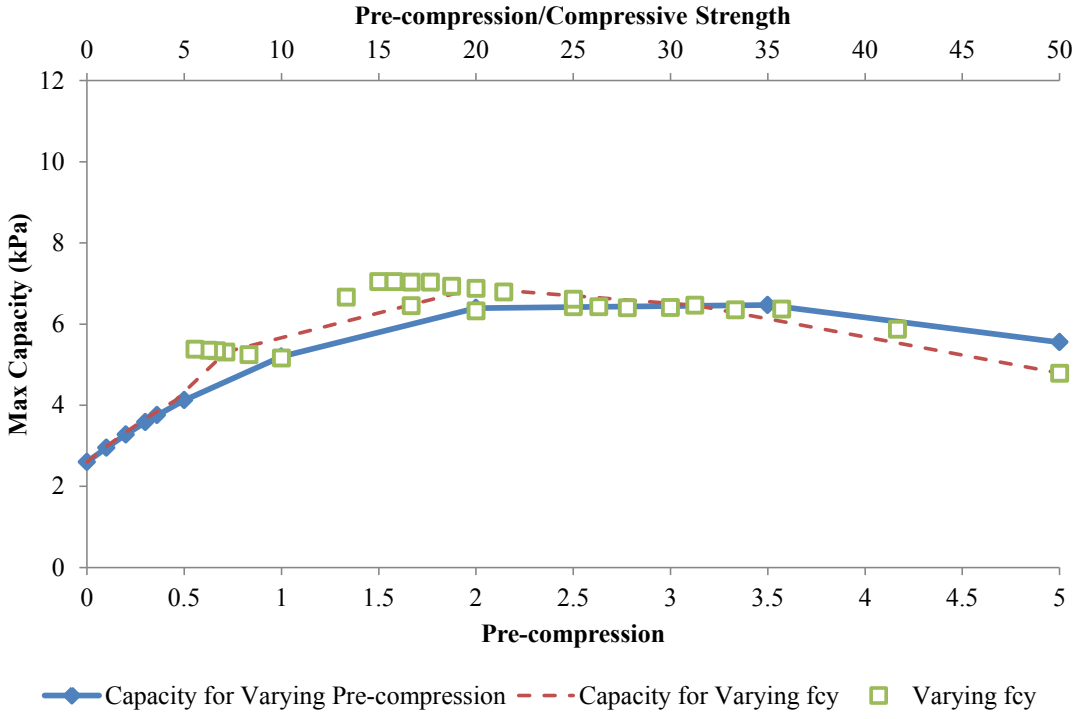

(d) Maximum Capacity Vs Pre-compression Graph

Fig. 16 Analysis of walls under pre-compression

The displacement ductility and the initial stiffness were calculated as $\mu = \Delta_u / \Delta_y$ and $K_0 = 0.8F_u / \Delta_y$, respectively. From the parametric study [shown in Fig. 16 (b)], the initial elastic stiffness K_o showed a curvilinear increasing pattern (up to77%) until σ_v reached

$1MPa$, followed by a linear decreasing pattern under higher pre-compression. The initial stiffness corresponding to zero and $1MPa$ pre-compression were 3900 N/mm and 6880 N/mm, respectively. A close prediction of K_o value is found at $\sigma_v = 0.1MPa$, where the EFE model and experimental investigation [22] showed initial stiffness of 4900 N/mm and 4210 N/mm, respectively.

Fig. 16 (c) shows a sensitive relationship between the displacement ductility (μ) corresponding to 20% strength degradation and pre-compression (σ_v). An insight into the result shows that the displacement ductility (μ) corresponding to zero pre-compression was 4.5, that linearly increased up to 8.5 for $\sigma_v \leq 0.5MPa$. Further increase in vertical pre-compression showed a rapid decrease in ductility.

Fig. 16 (d) shows the relation between maximum capacity of the wall with normalised pre-compression loading, where the normalised pre-compression is represented in terms of percentage of the compressive strength of masonry (f_{cy}). At zero vertical loading the capacity of the wall was 2.6 MPa which increased with the increase in σ_v. The maximum capacity of the wall was 6.4 kPa, which was within 20~30% of σ_v/f_{cy} (between 2~3MPa pre-compression). The out-of-plane capacity showed a gradually decreasing pattern as σ_v/f_{cy} exceeded this range [20~30%]. The relation shown in Fig. 16 (d) by solid line was obtained from increasing pre-compression σ_v for the same material properties. To further cross-check the relation, f_{cy} was varied with constant σ_v to generate another series ofσ_v/f_{cy}, shown by the independent bullet points in Fig. 16 (d). The average values of these independent bullet points are connected by a dashed line that yielded an identical relationship between capacity and normalised pre-compressionσ_v/f_{cy}.

The influence of pre-compression on walls with varying aspect ratio is shown in Fig. 17. A generalised trend is observed in the displacement ductility and the maximum capacity of the walls irrespective of the aspect ratio. Exception, walls with *H/L*=1.6 showed an inverted relation for stiffness over other walls.

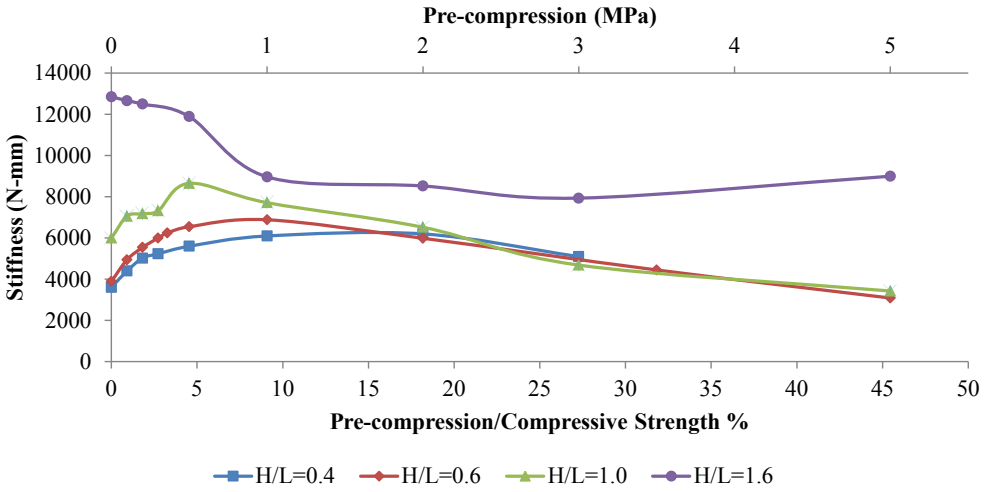

(a) Influence on stiffness

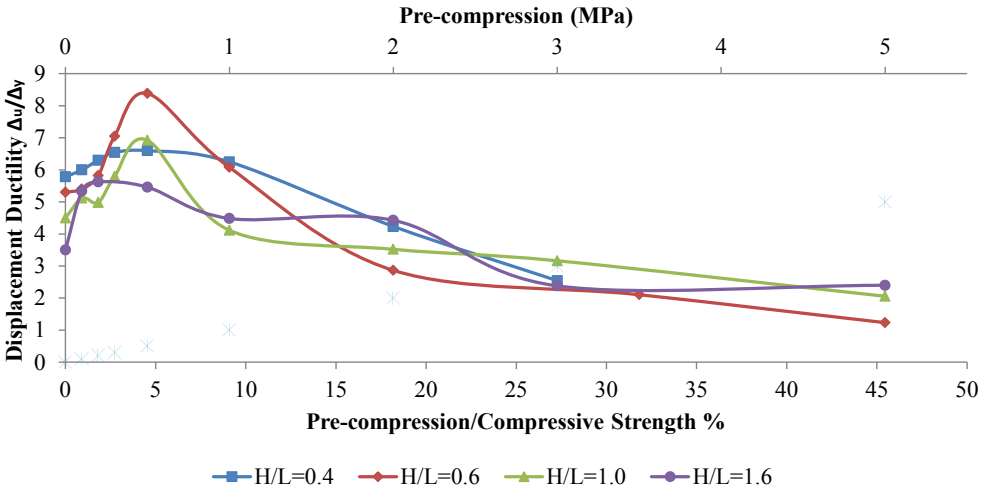

(b) Influence on displacement ductility

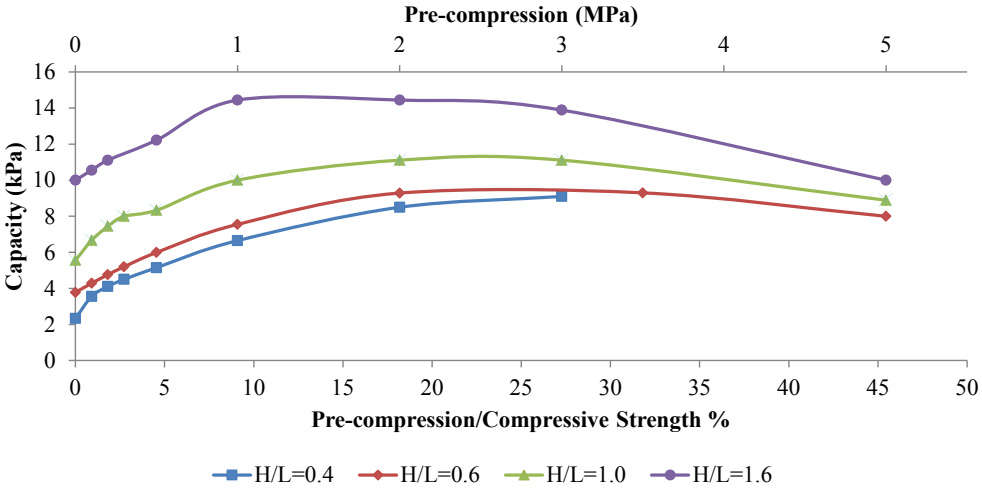

(c) Influence on maximum capacity

Fig.17 Effect of pre-compression on walls with varying aspect ratio

7 Conclusion

An explicit finite element model for 3D shell element has been developed for predicting the out-of-plane behaviour of masonry. The VUMAT masonry material model has updated for the 3D shell element. The EFE model successfully predicted the out-of-plane behaviour of URM walls. The following conclusions are drawn from the study:

- The developed explicit EFE macro modelling approach is used in modelling the out-of-plane flexural response of a URM solid wall and the EFE model parameters had been calibrated. The calibrated EFE model had been used to validate the experimental out-of-plane response of walls under pre-compression and with openings, and the results compared well with the experimental outcomes.
- Since the model uses a layered shell element, masonry of various forms (reinforced, grouted, surface rendered) can be analysed. Work is in progress for such application.
- Since shell element formulation is used, multi-directional loading for combined in-plane; out-of-plane and pre-compression actions can be modelled.
- An element size of 120mm square was found satisfactory to represent the homogenised masonry; for out-of-plane response studies, the calibrated masonry properties except the flexural tensile bond strength of masonry were not quite sensitive. The EFE model could therefore be adopted with only the flexural tensile bond strength representative of any masonry.
- The localised stress-strain relation has been studied along both parallel and normal to bed joint directions. It is found that strain normal to bed joint at the mid-span suddenly increased after the stress reached the input value which caused vertical crack widening at mid-span. The stress-strain contour plot also identified the two-way cracking pattern, with the development of zigzag cracks along the diagonal from a combination of increasing horizontal and vertical strains.
- Walls with returns and 4-side supported walls were 98% and 38% stronger respectively, than 2-side supported walls. The 4-side supported wall showed the highest ductility compared with that of the other walls.
- The taller wall (H/L=1.6) showed 67% higher capacity than the square wall (H/L=1.0) and the longer wall (H/L=0.45) showed 50% lower capacity than the square wall. The ductility of the specimens showed an increasing trend with decreasing H/L ratio.
- The effect of pre-compression on the out-of-plane response has been studied. It was found that the initial stiffness of the wall showed a decreasing trend as the pre-

compression exceeded 1MPa. However, the maximum out-of-plane capacity degraded as pre-compression surpassed 20% of the compressive strength of the wall. The displacement ductility increased until 0.5 MPa pre-compression.

- As explicit FE formulation is used, the model could also be applied for various impact simulations.

Acknowledgements

The scholarship support and the tuition award to the first author from Queensland University of Technology (QUT) is greatly acknowledged. The authors also gratefully acknowledge the desktop and software provided by QUT and high performance computing support from the HPC team.

References

[1] Dhanasekar M, Haider W. Explicit finite element analysis of lightly reinforced masonry shear walls. Computers & Structures. 2008;86:15-26.
[2] Nazir S, Dhanasekar M. A non-linear interface element model for thin layer high adhesive mortared masonry. Computers & Structures. 2014;144:23-39.
[3] Janaraj T, Dhanasekar M. Finite element analysis of the in-plane shear behaviour of masonry panels confined with reinforced grouted cores. Construction and Building Materials. 2014;65:495-506.
[4] Nazir S. Studies on the failure of unreinforced masonry shear walls. PhD Thesis, Queensland University of Technology, Brisbane, Australia; 2015.
[5] Shawa OA, Felice G, Mauro A, Sorrentino L. Out-of-plane seismic behaviour of rocking masonry walls. Earthquake Engineering & Structural Dynamics. 2012;41:949-68.
[6] Felice GD, Giannini R. Out-of-plane seismic resistance of masonry walls. Journal of Earthquake Engineering. 2001;5:253-71.
[7] Freidenberg A, Aviram A, Stewart L, Whisler D, Kim H, Hegemier G. Demonstration of tailored impact to achieve blast-like loading. International Journal of Impact Engineering. 2014;71:97-105.
[8] Berto L, Saetta A, Scotta R, Vitaliani R. An orthotropic damage model for masonry structures. International Journal for Numerical Methods in Engineering. 2002;55:127-57.
[9] Ferreira TM, Costa AA, Vicente R, Varum H. A simplified four-branch model for the analytical study of the out-of-plane performance of regular stone URM walls. Engineering Structures. 2015;83:140-53.
[10] Cavaleri L, Fossetti M, Papia M. Modeling of out-of-plane behavior of masonry walls. Journal of Structural Engineering (ASCE). 2009;135:1522-32.
[11] Griffith MC, Lam NT, Wilson JL, Doherty K. Experimental investigation of unreinforced brick masonry walls in flexure. Journal of Structural Engineering (ASCE). 2004;130:423-32.
[12] Bernat-Maso E, Gil L, Roca P. Numerical analysis of the load-bearing capacity of brick masonry walls strengthened with textile reinforced mortar and subjected to eccentric compressive loading. Engineering Structures. 2015;91:96-111.

[13] Rafsanjani SH, Lourenço P, Peixinho N. Dynamic interface model for masonry walls subjected to high strain rate out-of-plane loads. International Journal of Impact Engineering. 2015;76:28-37.
[14] Macorini L, Izzuddin B. Nonlinear analysis of unreinforced masonry walls under blast loading using mesoscale partitioned modeling. Journal of Structural Engineering (ASCE). 2014;140.
[15] Drougkas A, Roca P, Molins C. Numerical prediction of the behavior, strength and elasticity of masonry in compression. Engineering Structures. 2015;90:15-28.
[16] Milani G, Lourenço P, Tralli A. Homogenization approach for the limit analysis of out-of-plane loaded masonry walls. Journal of Structural Engineering (ASCE). 2006;132:1650-63.
[17] Su Y. Numerical simulation of strengthened unreinforced masonry (URM) walls by new retrofitting technologies for blast loading. Masters Thesis, University of Adelaide, Australia; 2009.
[18] Gattulli V, Lampis G, Marcari G, Paolone A. Simulations of FRP reinforcement in masonry panels and application to a historic facade. Engineering Structures. 2014;75:604-18.
[19] Dhanasekar M, Page A, Kleeman P. The failure of brick masonry under biaxial stresses. ICE Proceedings: Thomas Telford; 1985b. p. 295-313.
[20] Lourenço PB. Anisotropic softening model for masonry plates and shells. Journal of Structural Engineering (ASCE). 2000;126:1008-16.
[21] Hibbitt H, Karlsson B, Sorensen P. Abaqus analysis user's manual version 6.10. Dassault Systèmes Simulia Corp Providence, RI, USA. 2011.
[22] Vaculik J. Unreinforced masonry walls subjected to out-of-plane seismic actions. PhD Thesis, University of Adelaide, Adelaide, Australia; 2012.
[23] Mercatoris B, Massart T. A coupled two-scale computational scheme for the failure of periodic quasi-brittle thin planar shells and its application to masonry. International Journal for Numerical Methods in Engineering. 2011;85:1177-206.
[24] Shedid MT, Drysdale RG, El-Dakhakhni WW. Behavior of fully grouted reinforced concrete masonry shear walls failing in flexure: Experimental results. Journal of Structural Engineering (ASCE). 2008;134:1754-67.